A Systematic Comparison between 1-D and 3-D Hemodynamics in Compliant Arterial Models

Nan Xiao[1,2,◦], **Jordi Alastruey**[1,◦], and **C. Alberto Figueroa**[1,*]

[1]Department of Biomedical Engineering, King's College London, UK

[2]Department of Bioengineering, Stanford University, CA, USA

SUMMARY

In this article, we present a systematic comparison of computational hemodynamics in arterial models with deformable vessel walls using a one-dimensional (1-D) and a three-dimensional (3-D) method. The simulations were performed using a series of idealized compliant arterial models representing the common carotid artery, thoracic aorta, aortic bifurcation, and full aorta from the arch to the iliac bifurcation. The formulations share identical outflow boundary conditions and have compatible material laws. We also present an iterative algorithm to select the parameters for the outflow boundary conditions using the 1-D theory to achieve a desired systolic and diastolic pressure at a particular vessel. This 1-D/3-D framework can be used to efficiently determine material and boundary condition parameters for 3-D subject-specific arterial models with deformable vessel walls. Finally, we explore the impact of different anatomical features and hemodynamic conditions on the numerical predictions. The results show good agreement between the two schemes, especially during the diastolic phase of the cycle.

1. INTRODUCTION

One-dimensional (1-D) and three-dimensional (3-D) formulations have been used extensively to simulate arterial hemodynamics. Landmark contributions in 1-D modeling include the works of Hughes and Lubliner [1], Stergiopulos *et al.* [2, 3], Olufsen *et al.* [4], Formaggia *et al.* [5], Sherwin *et al.* [6], Bessems *et al.* [7], Mynard and Nithiarasu [8], Alastruey *et al.* [9], and Müller and Toro [10]. Key contributions to 3-D blood flow modeling in deformable vessels include the works of Perktold *et al.* [11], Taylor *et al.* [12], Quarteroni *et al.* [13], Steinman *et al.* [14], Cebral *et al.* [15], Gerbeau *et al.* [16], and Figueroa *et al.* [17]. 1-D methods have been used to improve our theoretical understanding

*Correspondence to: 3rd Floor Lambeth Wing, St Thomas' Hospital, King's College London, London SE1 7EH, UK, Telephone: +44 771 580 2408, Fax: +44 207 188 5442, alberto.figueroa@kcl.ac.uk.
◦: These authors contributed equally to this work

of hemodynamics, in particular to study the mechanisms underlying pulse wave propagation [18, 19] and also clinically in applications such as wave intensity analysis [20]. Accurate predictions can be made when when the flow is predominantly unidirectional and there are no sudden changes in cross-sectional area. However, 1-D models require the introduction of additional empirical laws to account for recirculation and pressure losses in the presence of vessel curvatures, stenoses, aneurysms, etc. [2, 21, 22] These geometric complexities are intrinsically captured with 3-D models, which can provide localized hemodynamic quantities such as wall shear stress, particle residence time, etc. Additionally, 3-D modeling enables the use of structurally-motivated biaxial constitutive laws [23] and circumferentially-varying mechanical properties for the arterial wall [24] and the simulation of complex processes such as the interactions between the arterial wall and medical devices [25, 26]. Nevertheless, 1-D models typically contain far fewer degrees of freedom in comparison to 3-D models (on the order of 10^3 versus 10^6) and the simulations can be executed in a matter of minutes on a personal laptop computer.

Previous works have compared 1-D models and 3-D models with rigid walls in the context of cerebral arterial flow [27, 28] and with deformable vessels in the aorta under steady flow [29]. However, a systematic comparison between 1-D and 3-D models in a variety of deformable arterial configurations was still missing in the literature. In general, a good agreement between the two modeling techniques is expected when the flow is mostly unidirectional and there are no sudden changes in cross-sectional area, while larger differences are expected in more complex configurations, such as in curved vessels and areas with highly dynamic flows. For a proper comparison to be made, a framework containing the 1-D and 3-D formulations that share equivalent boundary conditions and material laws must be developed. In general, this framework can be used to quickly estimate boundary condition parameters and distributions of material coefficients for an extensive multi-branched 3-D model (e.g. a full-body scale arterial network model [30]), a task that is more time-consuming in the isolated 3-D setting. The purpose of this paper is twofold:

1. To perform a systematic comparison between cross-sectionally-averaged hemodynamics (i.e. average flow, average pressure and radial deformation) obtained with two specific implementations of the 1-D and 3-D formulations in a series of four increasingly complex idealized geometries representing the common carotid artery, the thoracic aorta, the aortoilliac bifurcation and the full aorta including the first generation of branches. This simplified set of geometries, as opposed to patient-specific geometries, allows for a more direct comparison between the 1-D and 3-D schemes. We investigated the differences in the hemodynamic predictions introduced by increased Reynolds number, the presence of tapering, curvature, and bifurcation angles. To ensure a consistent comparison between formulations, we used equivalent constitutive laws in the 1-D and 3-D formulations, imposed identical flow waveforms and velocity profiles at the inlets, and coupled three-element Windkessel models at the outlets. In these comparisons, the 1-D geometric parameters were obtained directly using dimensions taken from the idealized 3-D geometries (see Fig. 1).

2. To develop a computational framework where a 1-D model is used to quickly determine boundary condition and material parameters to match patient data such as flow and pressure waveforms and localized measurements of distensibility. Once evaluated, the parameters are fed directly to the 3-D model to perform localized studies. Our aim is to exploit the advantages of both schemes: a computationally efficient 1-D model combined with a full 3-D model sharing identical boundary condition and constitutive laws. This overlapping 3-D/1-D approach can potentially accelerate the solution turn-around time of complex 3-D models, therefore improving their clinical applicability, and differs from previous efforts [13, 31, 32, 33] where 3-D and 1-D models were coupled to represent spatially distinct parts of the arterial tree.

The structure of this paper is as follows: we first present the details of the 1-D and 3-D formulations utilized in this work, paying special attention to the description of boundary conditions and material laws that are consistent between the two approaches. We then compare the numerical predictions of both methods in a series of idealized geometries. Finally, we describe and discuss the similarities and differences in the results between the two formulations and finish with conclusions and future work.

2. METHODS

2.1. One-dimensional Formulation

Conservation of mass and momentum applied to a 1-D impermeable and deformable tubular control volume of an incompressible Newtonian fluid yields [6, 34, 19]

$$\begin{cases} \frac{\partial A}{\partial t} + \frac{\partial (AU)}{\partial x} = 0 \\ \frac{\partial U}{\partial t} + U\frac{\partial U}{\partial x} + \frac{1}{\rho_f}\frac{\partial P}{\partial x} = \frac{f}{\rho_f A} \end{cases}, \quad (1)$$

where x is the axial coordinate along the vessel, t is the time, $A(x, t)$ is the cross-sectional area of the lumen, $U(x, t)$ is the axial blood flow velocity averaged over the cross-section, $P(x, t)$ is the blood pressure averaged over the cross-section, ρ_f is the density of blood assumed to be constant and $f(x, t)$ is the frictional force per unit length. The momentum correction factor in the convection acceleration term of Eq. (1) was assumed to be equal to one, following the work of Stergiopulos *et al*. [2]. Equation (1) can also be derived by integrating the incompressible Navier-Stokes equations over a generic cross section of a cylindrical domain [1, 35, 36, 37].

In this work, the velocity profile is assumed to be constant in shape and axisymmetric. The axial velocity (u) is assumed to have the shape

$$u(x, \xi, t) = U(x, t)\frac{\zeta+2}{\zeta}\left[1 - \left(\frac{\xi}{r}\right)^{\zeta}\right], \quad (2)$$

where $r(x, t)$ is the lumen radius, ξ is the radial coordinate and ζ is the polynomial order. Following [35], $\zeta = 9$ provides a good compromise fit to experimental data obtained at different points in the cardiac cycle.

Integration of the Navier-Stokes equations of an incompressible Newtonian fluid for axisymmetric vessels yields $f(x, t) = 2\mu\pi r \frac{\partial u}{\partial \xi}|_{\xi=r}$ [35]. For the velocity profile given by Eq. (2) we have $f = -2(\zeta + 2)\mu\pi U$ in which the local f is proportional to the local flow. Note that $\zeta = 2$ leads to the Poiseuille flow resistance $f = -8\mu\pi U$. For all of the simulations presented, $\mu = 4$ mPa s and $\rho_f = 1060$ kg/m^3.

An explicit algebraic relationship between P and A (or *tube law*) is also required to close Eq. (1) and account for the fluid-structure interaction of the problem. In general we have $P = \mathcal{A}$ $(A(x, t); x, t)$, where the function $\mathcal{A}$ depends on the model used to describe the dynamics of the arterial wall.

We solved Eqs. (1) with the elastic tube law described in Section 2.3 using a discontinuous Galerkin scheme with a spectral/*hp* spatial discretization and a second-order Adams-Bashforth time discretization [9]. The initial conditions are $(A(x, 0), U(x, 0), P(x, 0)) = (A_0(x), 0, 0)$, where A_0 is the initial area that yields A_d at $P = P_d$, with P_d the diastolic pressure. In all our 1-D simulations we implemented boundary conditions and solved matching conditions at bifurcations by taking into account the correct propagation of the characteristic information and neglecting energy losses [19, 38].

2.2. Three-dimensional Formulation

The coupled-momentum method [17] is used to formulate the 3-D FSI problem. Here, the degrees of freedom for the vessel wall (displacements $\boldsymbol{u}$) are described as a function of the fluid velocities at the fluid-wall interface, Σ, using an "enhanced" membrane formulation. Under the assumption of a fixed fluid domain, i.e. linearized kinematics of the vessel wall, the strong form is defined in an Eulerian configuration:

$$
\begin{aligned}
\rho_f(\dot{\boldsymbol{v}} + \boldsymbol{v} \cdot \nabla \boldsymbol{v}) &= -\nabla p + \nabla \cdot \tau_f + \boldsymbol{b} &\text{in} \quad \Omega^f, \\
\nabla \cdot \boldsymbol{v} &= 0 &\text{in} \quad \Omega^f, \\
\boldsymbol{v} &= \boldsymbol{v}_s &\text{on} \quad \Sigma,
\end{aligned}
\tag{3}
$$

$$
\begin{aligned}
\rho_s \dot{\boldsymbol{v}}_s - \nabla \cdot \boldsymbol{\sigma}_s &= \frac{1}{h} f_{\text{support}} &\text{in} \quad \Sigma \times h, \\
\boldsymbol{\sigma}_s \cdot \boldsymbol{n}_s &= (-p\boldsymbol{I} + \tau_f) \cdot \boldsymbol{n}_s
\end{aligned}
\tag{4}
$$

where Ω^f denotes the fluid domain, $\boldsymbol{v}$ is the fluid velocity, p is the pressure, $\boldsymbol{b}$ is a body force (here, assumed to be zero), and $\tau_f = \mu(\nabla\boldsymbol{v} + (\nabla\boldsymbol{v})^T)$ is the viscous stress tensor for a Newtonian fluid. The arterial wall is treated as a thin membrane with thickness h and density ρ_s where $\boldsymbol{v}_s$ is the solid velocity, $\boldsymbol{\sigma}_s$ is the membrane stress tensor, and $\boldsymbol{n}_s$ is the outward normal at the fluid-wall interface. The value of ρ_s was 0.001 g/mm^3 for all models.

To account for the mechanical forces exerted by the external tissues on the arterial walls, an additional term, $f_{\text{support}} = (k_s\boldsymbol{u} + c_s\boldsymbol{v})$, was included in Eq. (4) which approximates the mechanical behavior of the external tissue [39], where the parameters k_s and c_s are the

stiffness and damping coefficients. This additional force can be used to eliminate spurious and nonphysiological oscillations in specific cases where the geometry is elongated and the vessel wall experiences asymmetric loads. For the simulations presented in this paper, unless explicitly stated, the values of k_s and c_s are set to zero.

With the assumption that the vessel wall thickness (h) is small and with appropriate choices for the solution and test function spaces, $\mathcal{S}$, $\mathcal{P}$ and $\mathcal{W}$, the strong form gives rise to the variational equation:

$$
\begin{aligned}
&\int_{\Omega^f}\{\boldsymbol{w}\cdot(\rho_f\,\dot{\boldsymbol{v}}+\rho_f\boldsymbol{v}\nabla\,\boldsymbol{v}-\boldsymbol{b})+\nabla\,\boldsymbol{w}:(-p\boldsymbol{I}+\boldsymbol{\tau}_f)-\nabla\,q\cdot v\}dv \\
&\quad+\int_{\Gamma_{in}}q\boldsymbol{v}\cdot\boldsymbol{n}_f da-\int_{\Gamma_{out}}\boldsymbol{w}\cdot\boldsymbol{h}da+\int_{\Gamma_{out}}q\boldsymbol{v}\cdot\boldsymbol{n}_f da \\
&\quad+\int_{\sum}\{h\rho_s\boldsymbol{w}\cdot\dot{\boldsymbol{v}}+h\nabla\,\boldsymbol{w}:\boldsymbol{\sigma}_s+\boldsymbol{w}\cdot(k_s\boldsymbol{u}+c_s\boldsymbol{v})+q\boldsymbol{v}\cdot\boldsymbol{n}_f\}da=0 \\
&\qquad\forall\boldsymbol{x}\in\overline{\Omega^f},\forall t\in[0,T],
\end{aligned}
\quad(5)
$$

where $\boldsymbol{w}\in\mathcal{W}$ and $q\in\mathcal{P}$ are test functions. Γ_{in} is a Dirichlet boundary where the test functions $\boldsymbol{w}$ vanish and where the fluid velocities are prescribed, i.e. at the inlet. The traction term $\boldsymbol{h}(v, p)$ on the outlet boundary Γ_{out} is given as a function of $\boldsymbol{v}$ and p depending on the reduced-order model (i.e. three-element Windkessel) chosen to represent the downstream vasculature, as described by Vignon-Clementel *et al*. [40, 41]. The augmented Lagrangian scheme described by Kim*et al*. [42] was used to stabilize the outflow velocities in the presence of flow reversal at the outflow boundaries.

To discretize and solve Eq. (5), we employed a stabilized semi-discrete finite element method based on the work of Brooks and Hughes [43], Franca and Frey [44], Taylor *et al*. [12], and Whiting and Jansen [45], using equal-order interpolation (P1/P1 elements) for the velocity and pressure fields. The generalized α-method [46, 47] was used to integrate the system of ordinary differential equations resulting from the finite element discretization.

2.3. Material Laws

The arterial wall was modeled as a thin, incompressible, homogeneous, isotropic, linear elastic membrane characterized by an elastic modulus E, a Poisson's ratio $\nu = 0.5$, and a thickness h.

In the 1-D model, the arterial wall is assumed to deform axisymmetrically, each cross-section independently of the others, so that the relationship between circumferential hoop stress, T_θ, and radial displacement is

$$
T_\theta=\frac{E}{1-\nu^2}\frac{r-r_d}{r_d}, \quad(6)
$$

where r_d is the radius at diastolic pressure (P_d). Applying Laplace's law, $T_\theta = (P - P_d)r/h$, and assuming that $1/r$ can be approximated by $1/r_d$, we obtain the tube law [9]

$$
P=P_d+\frac{4}{3}Eh\frac{r-r_d}{(r_d)^2}=P_d+\frac{\beta}{A_d}(\sqrt{A}-\sqrt{A_d}), \quad \beta=\frac{4}{3}\sqrt{\pi}Eh, \quad(7)
$$

where $A_d(x)$ is the luminal area at diastolic pressure. In Eq. (7), both E and h are functions of the position x. The pulse wave speed $c(x, t)$ is related to A through

$$c = \sqrt{\frac{\beta}{2\rho_f A_d}} A^{1/4}. \quad (8)$$

The initial area A_0 is calculated by replacing $P = 0$ and $A = A_0$ in Eq. (7), which leads to

$$A_0 = A_d \left(1 - \sqrt{A_d}\frac{P_d}{\beta}\right)^2. \quad (9)$$

In the 3-D formulation, no assumptions regarding axisymmetry were made. The enhanced membrane stress tensor $\tilde{\sigma}_s$ is given as a function of a tensor $\tilde{K}$ of material parameters, a tensor $\tilde{P}$ describing the pre-stress of the wall, and the infinitesimal strain tensor $\tilde{\varepsilon}$; $\tilde{\sigma}_s = \tilde{K}\tilde{\varepsilon}$, with

$$\tilde{K} = \frac{E}{1-\nu^2}\begin{pmatrix} 1 & \nu & 0 & 0 & 0 \\ \nu & 1 & 0 & 0 & \\ 0 & 0 & 0.5(1-\nu) & 0 & 0 \\ 0 & 0 & 0 & 0.5k(1-\nu) & 0 \\ 0 & 0 & 0 & 0 & 0.5k(1-\nu) \end{pmatrix}, \quad (10)$$

$$\tilde{\varepsilon} = \begin{pmatrix} \partial u_1/\partial x_1 \\ \partial u_2/\partial x_2 \\ \partial u_1/\partial x_2 + \partial u_2/\partial x_1 \\ \partial u_3/\partial x_1 \\ \partial u_3/\partial x_2 \end{pmatrix}, \quad \tilde{P} = \begin{pmatrix} P_{11} \\ P_{22} \\ P_{12} \\ P_{31} \\ P_{32} \end{pmatrix}, \quad (11)$$

where k is a transverse shear factor and u is the displacement vector [48]. In general, the pre-stress tensor can be specified using a variety of methods (see [39, 48, 49]). In the case of linear elasticity, the "pre-stress" can be incorporated by subtracting a reference displacement (i.e. at diastole) from the displacement field.

2.4. Boundary Conditions

The inlet and outlet boundary conditions were chosen to be consistent between the 1-D and 3-D schemes. At the inlet, we prescribed a known flow rate with an axisymmetric velocity profile (Eq. (2)). At the outlet of each terminal vessel, we coupled a three-element Windkessel model (Fig. 1). This zero-dimensional (0-D) electrical circuit analogue of the downstream vasculature consists of a resistance (R_1) connected in series with a parallel combination of a second resistance, (R_2), and a compliance, (C); P_{out} is the pressure at which flow to the microcirculation ceases and is assumed to be zero in all models. Pressure and the flow at an outlet of the 1-D or 3-D domain is related by

$$Q\left(1+\frac{R_1}{R_2}\right)+CR_1\frac{\partial Q}{\partial t}=\frac{P-P_{\text{out}}}{R_2}+C\frac{\partial P}{\partial t}. \quad (12)$$

The numerical implementation of this 0-D model is detailed in [19, 38] for the 1-D formulation and [41] for the 3-D formulation.

2.5. Iterative Procedure for the Determination of Outflow Windkessel Parameters

The parameters of the three-element Windkessel outflow models were calculated as described below. Given a target diastolic (P_d) and systolic (P_s) pressure, and flow rate at the inlet ($Q_{\text{in}}(t)$), the initial estimate for the net peripheral resistance (R_T) was calculated as [50]

$$R_T=\frac{P_m-P_{\text{out}}}{\overline{Q}_{\text{in}}}, \quad P_m=P_d+\frac{1}{3}(P_s-P_d), \quad (13)$$

where $\overline{Q}_{\text{in}}$ is the mean flow rate and P_m is the mean blood pressure, assumed uniform throughout the arterial network. We then calculated the resistance $R_1 + R_2$ at the outlet of each terminal vessel that yields the desired flow distribution and satisfies

$$\frac{1}{R_T}=\sum_{j=2}^{M}\frac{1}{R_1^j+R_2^j}, \quad (14)$$

where M is the number of terminal branches and $j = 1$ corresponds to the aortic root. For each individual outlet, the proximal resistance (R_1) is assumed to be equal to the characteristic impedance of the upstream 1-D domain; i.e.

$$R_1=\frac{\rho_f c_d}{A_d}, \quad (15)$$

where c_d and A_d are, respectively, the wave speed and area at diastolic pressure (P_d). This choice of R_1 minimizes the magnitude of the waves reflected at the outlet of the 1-D domain [38].

The total compliance (C_T) was calculated from either (i) the time constant $\tau = 1.79$ s of the exponential fall-off of pressure during diastole given in [51] or (ii) using an approximation to $C_T=\frac{dV}{dP}$, where $V(t)$ is the total blood volume contained in the systemic arteries. According to [50],

$$C_T=\frac{\tau}{R_T}, \quad (16)$$

which can be calculated once R_T is determined using Eq. (13). Alternatively, $C_T=\frac{dV}{dP}$ can be approximated by [50]

$$C_{\mathrm{T}} = \frac{Q_{\max} - Q_{\min}}{P_{\mathrm{s}} - P_{\mathrm{d}}} \Delta t, \quad (17)$$

where $Q_{\max}$ and $Q_{\min}$ are the maximum and minimum flow rates at the inlet and t is the difference between the time at $Q_{\max}$ and the time at $Q_{\min}$. We use both Eqs. (16) and (17) depending on the available input data.

According to [52] we have

$$C_{\mathrm{T}} = C_{\mathrm{c}} + C_{\mathrm{p}}, \quad C_{\mathrm{c}} = \sum_{i=1}^{N} C_{0\mathrm{D}}^i, \quad C_{\mathrm{p}} = \sum_{j=2}^{M} \frac{R_2^j C^j}{R_2^j + R_1^j}, \quad (18)$$

where C_{c} is the total arterial conduit compliance, C_{p} is the total arterial peripheral compliance, N is the total number of vessels in the 1-D domain, $M < N$ is the number of terminal branches ($j = 1$ denotes the inlet and is not included in the sum), R_1, R_2, and C are parameters of the three-element Windkessel model (Fig. 1) and $C_{0\mathrm{D}}$ is the compliance of each vessel, which is calculated as

$$C_{0\mathrm{D}} = \frac{A_{\mathrm{d}} L}{\rho_{\mathrm{f}} (c_{\mathrm{d}})^2}, \quad (19)$$

where L is the length of the vessel. We calculated $C_{\mathrm{p}} = C_{\mathrm{T}} - C_{\mathrm{c}}$ and distributed it following the methodology described by Alastruey et al. [52] More specifically, we have

$$\tilde{C}^j = C_p \frac{R_{\mathrm{T}}}{R_2^j + R_1^j}, \quad (20)$$

where $\tilde{C^j}$ is the terminal compliance of each branch distributed in proportion to flow as described by Stergiopulos et al. [2]. We then introduced a correction factor to arrive at the final value of C^j:

$$C^j = \tilde{C}^j \frac{R_2^j + R_1^j}{R_2^j} = C_{\mathrm{p}} \frac{R_{\mathrm{T}}}{R_2^j}. \quad (21)$$

This expression follows from a linear analysis of the 1-D equations in a given arterial network in which each terminal branch is coupled to a three-element Windkessel model [52].

For all of the simulations, the Windkessel compliances and resistances (C^j, $j = 2, \ldots, M$), (R_1^j and R_2^j, $j = 2, \ldots, M$) were iteratively calculated to achieve physiologically realistic pressure ranges. To reach a desired pulse pressure ($P_{\mathrm{pulse}} = P_{\mathrm{s}} - P_{\mathrm{d}}$) and diastolic pressure (P_{d}) at a particular vessel, we calculated R_{T}^0 and C_{T}^0 given by Eqs. (13) and (16) or (17) using the iterative formulae

$$R_{\mathrm{T}}^{n+1}=R_{\mathrm{T}}^{n}+\frac{\Delta P_{\mathrm{m}}^{n}}{Q_{\mathrm{in}}}, \quad \Delta P_{\mathrm{m}}^{n}=P_{\mathrm{d}}-P_{\mathrm{d}}^{n}, \quad (22)$$

$$C_{\mathrm{T}}^{n+1}=C_{\mathrm{T}}^{n}-\frac{Q_{\max}-Q_{\min}}{(P_{\mathrm{pulse}}^{n})^{2}}\Delta t\Delta P_{\mathrm{pulse}}^{n}, \quad \Delta P_{\mathrm{pulse}}^{n}=P_{\mathrm{pulse}}-P_{\mathrm{pulse}}^{n}, \quad (23)$$

where the superscript n is the iteration number of the windkessel parameter estimation process performed using the 1-D formulation, and P_{d}^{n} and P_{pulse}^{n} are the diastolic and pulse pressure, respectively, at a specific target location in the 1-D model, typically the inlet, at each iteration. Equations (22) and (23) follow from a first-order Taylor expansion of Eqs. (13) and (17) around the current mean and pulse pressures P_{m}^{n} and P_{pulse}^{n}, respectively, with $\Delta P_{\mathrm{m}}^{n}$ approximated using the change in diastolic pressure. The total compliance was adjusted by altering the total peripheral compliance C_{p}, since the total conduit compliance C_{c} is a function of the vessel geometry and wall stiffness. This process was iterated using the 1-D model until P_{d}^{n} and P_{pulse}^{n} were smaller than 1% of the target P_{d} and P_{pulse}, respectively. Fig. 2 shows the evolution of the systolic, mean and diastolic pressure, net peripheral resistance and total compliance calculated using the 1-D formulation to match the target systolic and diastolic pressures for the baseline aorta model. The final values of the Windkessel compliances and resistances were used in the 3-D counterparts of the 1-D models.

Other methods have been proposed in the literature to estimate the parameters of the outflow boundary conditions. A root-finding method is described by Spilker and Taylor [53] in the context of 3-D models with compliant arterial walls. Devault *et al.* proposed a Kalman-filter based methodology in a 1-D model of the circle of Willis [54].

2.6. Error Calculations

The numerical solutions of pressure P and volumetric flow Q were compared between the 1-D and 3-D models using the following relative error metrics [9]:

$$\varepsilon_{P,\mathrm{avg}}=\frac{1}{N_{t}}\sum_{i=1}^{N_{t}}\left|\frac{P_{i}^{1\mathrm{D}}-P_{i}^{3\mathrm{D}}}{P_{i}^{3\mathrm{D}}}\right|, \quad \varepsilon_{Q,\mathrm{avg}}=\frac{1}{N_{t}}\sum_{i=1}^{N_{t}}\left|\frac{Q_{i}^{1\mathrm{D}}-Q_{i}^{3\mathrm{D}}}{\max_{j}(Q_{j}^{3\mathrm{D}})}\right|, \quad (24)$$

$$\varepsilon_{P,\max}=\max_{i}\left|\frac{P_{i}^{1\mathrm{D}}-P_{i}^{3\mathrm{D}}}{P_{i}^{3\mathrm{D}}}\right|, \quad \varepsilon_{Q,\max}=\max_{i}\left|\frac{Q_{i}^{1\mathrm{D}}-Q_{i}^{3\mathrm{D}}}{\max_{j}(Q_{j}^{3\mathrm{D}})}\right|, \quad (25)$$

$$\varepsilon_{P,\mathrm{sys}}=\frac{\max_{i}(P_{i}^{1\mathrm{D}})-\max_{i}(P_{i}^{3\mathrm{D}})}{\max_{i}(P_{i}^{3\mathrm{D}})}, \quad \varepsilon_{Q,\mathrm{sys}}=\frac{\max_{i}(Q_{i}^{1\mathrm{D}})-\max_{i}(Q_{i}^{3\mathrm{D}})}{\max_{i}(Q_{i}^{3\mathrm{D}})}, \quad (26)$$

$$\varepsilon_{P,\text{dis}} = \frac{\min_i(P_i^{1D}) - \min_i(P_i^{3D})}{\min_i(P_i^{3D})}, \qquad \varepsilon_{Q,\text{dias}} = \frac{\min_i(Q_i^{1D}) - \min_i(Q_i^{3D})}{\max_i(Q_i^{3D})}, \quad (27)$$

where N_t is the number of time points where the comparison is made (typically around several thousand points over a single cardiac cycle depending on the time step size), P_i^{1D}, Q_i^{1D} are the pressure and flow results at each time point i from the 1-D simulation at a single spatial location, and P_i^{3D}, Q_i^{3D} are the cross-sectional averaged pressure and flow at each time point i from the 3-D model at a single cross-section perpendicular to the vessel centerline. $\varepsilon_{P,\text{avg}}$ and $\varepsilon_{Q,\text{avg}}$ are the average relative errors for pressure and flow, respectively, over one cardiac cycle, and $\varepsilon_{P,\text{max}}$ and $\varepsilon_{Q,\text{max}}$ are the maximum relative error in pressure and flow. $\varepsilon_{P,\text{sys}}$ and $\varepsilon_{Q,\text{sys}}$ are the errors for systolic pressure and flow, $\varepsilon_{P,\text{dias}}$ and $\varepsilon_{Q,\text{dias}}$ are the errors for diastolic pressure and flow. In order to avoid division by small values of flow, we normalized the flow error metrics by the maximum value of flow over the cardiac cycle, $\max_i(Q_i^{3D})$. The error metrics were calculated over a single cardiac cycle once both numerical solutions achieved periodic behavior.

3. RESULTS

We investigated the differences in the numerical prediction of flow and pressure between the 1-D and 3-D formulations (where flow and pressure refer to cross-sectional averages in planes perpendicular to the vessel centerline) in a series of test cases using idealized geometries. The physical dimensions, vessel wall properties, and inflow and outflow boundary conditions were made to be consistent between the 1-D models and their 3-D counterparts. Mesh independence studies were undertaken to ensure that the results in the final meshes were not affected by inadequate mesh resolution.

3.1. Baseline Common Carotid

We considered a straight cylindrical vessel with representative dimensions of the common carotid artery (CCA). The initial total peripheral resistance (R_T) and compliance (C_T) were calculated from Eqs. (13) and (17), respectively, using a reference value of mean blood pressure (P_m) measured in a 23-year-old human [55, p. 343] and a reference inflow waveform [17]. The final values of R_T and C_T were then computed as described in Section 2.5, requiring a single iteration to achieve convergence to the target pressures at the outlet. The parameters of the CCA model are given in Table I.

The 1-D simulation was run using 6 elements with a quadrature and polynomial order of 10 and a time step of 0.1 ms. The velocity profile order was $\zeta = 2$. The initial area $A_0 = 0.22$ cm^2 that yields the reference diastolic area (A_d) at $P = P_d$ was calculated using Eq. (9). The 3-D geometry was constructed with the same dimensions as in the 1-D segment. The velocity on the inlet boundary was prescribed using Eq. (2) with $\zeta = 2$ and with the same time-averaged flow-rate as at the inlet of the 1-D model. The 3-D simulation was run with a mesh containing 792,559 linear tetrahedral elements (145,394 nodes) and a time-step of 0.2 ms.

Fig. 3 shows the numerical predictions of flow rate, pressure, changes in luminal radius, and velocity profiles at several sites in the 1-D and 3-D models. The flow waveforms exhibit the typical attenuation observed *in vivo* between the inlet and outlet faces. We also include the pressure gradient (given as the difference between inlet and outlet pressures) predicted by the two numerical schemes. The results show excellent agreement between the two models, with average relative errors smaller than 1%. However, even though the flow waveforms in 1-D and 3-D models are virtually identical, differences can be observed in the velocity profiles. These differences result from the linearized kinematics assumption (i.e. fixed computational domain) of the 3-D formulation, in contrast to the 1-D model, which accounts for changes in cross-sectional area. In all the examples considered in this manuscript, the 1-D velocity profiles were plotted in the reference configuration given by the nominal (diastolic) diameter of the vessel to provide a qualitative comparison between the profile shapes.

3.2. Baseline Aorta

We considered a straight cylinder with diameter representative of the average diameter of the thoracic aorta. Here, the initial peripheral resistance was calculated using systolic and diastolic pressures from [51] and the total compliance C_T was calculated from the time constant $\tau = 1.79$ s [51] of the exponential fall-off of pressure during diastole using Eq. (16). The final values of R_T and C_T were obtained after seven iterations to reach convergence to the target pressures at the outlet. The parameters of the baseline aortic model are given in Table II.

For the 1-D model, the simulation was run using 12 elements with a quadrature and polynomial order of 5 and a time step of 0.1 ms. The initial area was calculated using Eq. (9) to be $A_0 = 3.06$ cm^2. The polynomial order of the velocity profile was chosen to be $\zeta = 9$ based on [35]. For the 3-D model, the velocity boundary condition at the inlet was prescribed with a profile of order $\zeta = 9$. The 3-D simulation was run using a mesh containing 1,480,048 linear tetrahedral elements (261,912 nodes) and a time step of 0.2 ms.

Fig. 4 shows the numerical predictions of flow rate, pressure, changes in luminal radius, and velocity profiles at several sites in the 1-D and 3-D models. Fig. 4 also contains a plot of the pressure gradient between the inlet and outlet. The overall agreement between the two formulations is still reasonably good, particularly during diastole, with average relative errors smaller than 2%. The largest differences in pressure are seen at the inlet during acceleration, and the largest differences in flow are observed during peak systolic flow at the mid-point and outlet locations. The velocity contours at deceleration ($t = 0.33$ s) are markedly different: while the 1-D solution preserves the fixed 9th-order velocity profile, the 3-D results show near-wall flow reversal, resulting in a Womersley-like profile. Furthermore, the axisymmetry of the 3-D profile breaks down in the second half of the vessel during peak systole ($t = 0.15$ s). The pressure gradient plot shows larger absolute differences than in the carotid geometry and a slight phase-lag between the 3-D and 1-D predictions.

3.3. Low Flow, and Larger Diameter Aorta

To study the impact of Reynolds number and flow inertia, we considered two more cases in addition to the baseline straight aorta model. In the first case, the flow prescribed at the inlet was reduced by a factor of 9.54 to match the peak Reynolds number to that of the CCA model ($Re = 748$). In the second case, the diameter of the cylindrical domain was increased to 1.5 cm from 1.2 cm, while the flow rate and vessel length remained unchanged ($Re = 5$, 713 at peak systole). Figures 5 and 6 show the flow rate, pressure, change in luminal radius, and pressure gradient at several sites in the 1-D and 3-D models. While reducing the Reynolds number via decreasing the total flow did not decrease the error in the inlet pressures during acceleration (see Fig. 5), increasing the vessel diameter without altering the total flow (Fig. 6) did bring the 3-D and 1-D predictions closer.

3.4. Tapered Carotid

We considered a linearly tapered cylinder with the same length as the previous CCA geometry. Based on reference values for the degree of tapering of the left CCA in [56], the diameter was set to 8 mm at the inlet and 4 mm at the outlet. Although R_T remained unchanged from the non-tapered CCA model, the resistance R_1 (see Eq. (15)) was recalculated with the values of c_d and A_d at the location of the outlet, giving a value of $R_1 = 6.8548 \cdot 10^8$ Pa s m^{-3} and $R_2 = 1.4330 \cdot 10^9$ Pa sm^{-3}. The remaining parameters were unchanged from those given in Table I.

For the 1-D model, the velocity profile was specified with $\zeta = 2$ and the simulation was carried out using 6 elements with a quadrature and polynomial order of 10 and a time step of 0.1 ms. For the 3-D model, the velocity boundary condition at the inlet was prescribed using a profile of order $\zeta = 2$ and the simulation was run using a mesh containing 840,899 linear tetrahedral elements (153,539 nodes) and a time step of 0.2 ms.

Fig. 7 shows the flow rate, pressure, pressure gradient, velocity profiles and change in luminal radius at several sites in the 1-D and 3-D models. Slightly larger differences in 3-D/1-D predicted pressure are observed at the inlet and in the center of the vessel. Compared to the non-tapered CCA geometry, there is also a significant increase in pressure gradient discrepancy.

3.5. Tapered Aorta

We considered a linearly tapered cylinder with length identical to that of the baseline non-tapered aorta model. Based on typical reported aortic dimensions [56], the diameter was set to 3 cm at the inlet and 2 cm at the outlet. R_T remained unchanged from the baseline non-tapered aorta model, but the resistance R_1 was recalculated with the values of c_d and A_d at the location of the outlet. We obtained $R_1 = 1.8503 \cdot 10^7$ Pa s m^{-3} and $R_2 = 1.0492 \cdot 10^8$ Pa s m^{-3}. The remaining parameters were unchanged from those in Table II.

For the 1-D model, the polynomial order of the velocity profile was chosen to be $\zeta = 9$ and the 1-D simulation was run using 12 elements with a quadrature and polynomial order of 5 and a time step of 0.1 ms. For the 3-D model, the velocity boundary condition at the inlet boundary was prescribed using a profile of order $\zeta = 9$ and the simulation was run using a

mesh containing 1,663,772 linear tetrahedral elements (293,667 nodes) and a time step of 0.2 ms.

Fig. 8 shows the flow rate, pressure, changes in luminal radius, velocity profile, and pressure gradient at several sites in the 1-D and 3-D models. Results show larger differences in pressure and flow waveforms at the midpoint and inlet locations, respectively, compared to those found in the tapered carotid case. The differences between the velocity contours are also more noticeable, with the 3-D profile displaying near-wall flow-reversal patterns.

3.6. Aorta with Curvatures

We considered two additional aortic models using the same inflow and outflow boundary conditions as the baseline aorta model with the purpose of studying the impact of vessel curvature on cross-sectional average pressure and velocity. In the first case, curvature was introduced in a single plane (sagittal) to represent an idealized aortic arch. In the second case, curvatures were introduced in three planes (sagittal, coronal, and transverse) as described by Yearwood and Chandran [57]. Lengths and diameters were kept unchanged relative to the baseline aorta case. Since the 1-D model is independent of curvature, the 1-D solution is identical to that obtained in Section 3.2. The boundary conditions and material parameters were identical to those in the baseline aorta model (see Table II).

Due to the centripetal loading experienced by the vessel wall in the curved portion of the 3-D geometry, a small value for the external damping coefficient ($c_s = 300$ Pa s m^{-1}) was chosen to reduce nonphysiological oscillatory modes. The external damping smooths the pressure and flow waveforms predominantly where high frequencies are dominant, with distal waveforms being smoother than proximal ones. These results are in agreement with the linear analysis of wall viscoelasticity described in [50]. The simulation of the 3-D model containing the single plane of curvature was run using a mesh containing 1,691,525 linear tetrahedral elements (297,472 nodes) and a time step of 0.2 ms. The model containing three planes of curvature was simulated with a mesh containing 1,688,467 linear tetrahedral elements (297,083 nodes) and a time step of 0.2 ms.

Figures 9 and 10 show the flow rate, pressure, changes in luminal radius, and pressure gradient for the single-curvature and three-curvature cases, respectively, and compares them with the corresponding 1-D predictions, which are the same as those shown in Fig. 4. In-plane and out-of-plane velocity profiles at three cross sections in the 3-D models illustrate the skewing of the velocity profile toward the outer wall during systole and the presence of backflow along the inner wall during diastole. Nevertheless, the relative errors in flow, pressure, and pressure gradient are similar to those observed in the baseline aorta case.

3.7. Aortic Bifurcation

Here, we considered an idealized model of the aortic bifurcation, containing a single parent segment, representing the abdominal aorta, and two branch segments representing the iliac arteries. The lengths and diameters are listed in Table III. The initial net peripheral resistance and total compliance were calculated from Equations (13) and (17) using the systolic and diastolic pressures from [51]. The final values of R_T and C_T were obtained after

three iterations to reach convergence to the target pressures at the inlet. The peripheral resistance $R_1 + R_2$ at the outlet of the iliac arteries was calculated assuming equal flow distribution.

For the 1-D model, the simulation was run using 12 elements with a quadrature and polynomial order of 5 and a time step of 0.1 ms. The initial area was calculated using Eq. (9) to be $A_0 = 1.8062$ cm^2 in the abdominal aorta and $A_0 = 0.9479$ cm^2 in the iliac branches. The velocity profile was chosen to have a polynomial order $\zeta = 9$. For the 3-D model, the geometry was constructed from three cylinders with the same diameters and lengths as in the 1-D network. The angle between the two iliac branches was set to 47.9 degrees [58]. The velocity boundary condition at the inlet was prescribed with a profile of order $\zeta = 9$. The simulation was run using a mesh containing 1,799,117 linear tetrahedral elements (321,651 nodes) and a time step of 0.2 ms.

Fig. 11 shows the flow rate, pressure, velocity and changes in luminal radius at several sites in the 1-D and 3-D models. The results show excellent agreement between the two models (average relative errors smaller than 2%), with similar relative errors to the baseline common carotid artery case.

3.8. Full Aorta

We considered an idealized geometry representing the aorta and the first generation of main branches from just above the sinuses to the aortic bifurcation, neglecting the coronary and intercostal vessels. The curvature and angulation from the sagittal plane in the aortic arch were based on published measurements from human cadavers [57, 59]. The dimensions and spacing between branch vessels were based on those reported in [3]. The parameters are summarized in Table IV and the geometry is illustrated in Fig. 12. The spatially-varying elastic moduli (E) were calculated from the pulse wave velocity, c, given by the empirical relationship [56] $c = a_2/(2r_d)^{b_2}$, where c is given in m/s, r_d is the radius at diastolic pressure expressed in mm, $a_2 = 13.3$ and $b_2 = 0.3$. For each vessel segment, once c was determined, E was calculated using Eq. (8) with $A = A_d$. The spatially-varying wall thickness (h) was chosen to be 10% of r_d [55] at the inlet of each segment.

The total peripheral resistance $R_T = 1.1583 \cdot 10^8$ Pa s m^{-3} was obtained from Eq. (13) with $\bar{Q}_{in} = 6.17$ l min^{-1} $P_s = 16.8$ kPa and $P_d = 9.5$ kPa. At the outlet of each terminal branch, the resistance $R_1 + R_2$ was calculated to yield the flow distribution given in [2] (see Table V). Each resistance R_1 follows from Eq. (15) with c_d and r_d calculated at the outlet of the terminal branch. The total compliance C_T was calculated from the time constant $\tau = 1.79$ s [51] of the exponential fall-off of pressure during diastole using Eq. (16); $C_T = \tau/R_T = 1.5453 \cdot 10^{-8}$ m^3 Pa^{-1}. The compliance C of each terminal RCR model was then calculated as described in Section 2.5. The final values of R_T and C_T were obtained after eight iterations to reach convergence to the target pressures at the outlet of the abdominal aorta.

For the 1-D model, the simulation was run using 46 elements with a quadrature and polynomial order of 5 in each vessel and a time step of 0.05 ms. The initial areas A_0 that yield the diastolic areas A_d at $P = P_d$ were calculated using Eq. (9) ($A_0 = 4.7203$ cm^2 at the aortic root). The velocity profile was chosen with polynomial order $\zeta = 9$. For the 3-D

model, the external damping coefficient was assigned a small value ($c_s = 300$ Pa s m^{-1}) to reduce non-physiological oscillations. The simulation was run using a mesh containing 2,554,521 linear tetrahedral elements (475,000 nodes) and a time-step of 0.2 ms. The velocity boundary condition at the inlet was prescribed with a profile of order $\zeta = 9$.

Fig. 13 shows flow rate and pressure at a number of representative locations in the 1-D and 3-D models. The differences in the pressure and flow predictions occur predominantly in peak systole, and these discrepancies are greater in distal sites than in the proximal aortic arch branches. Additionally, the results from the 3-D model exhibit fewer high-frequency features in the flow and pressure waveforms than in the 1-D model as a consequence of external damping.

4. DISCUSSION

4.1. Carotid vs. Aortic Geometry: Combined Impact of Reynolds Number, Wall Strain and Velocity Profile

In the baseline carotid case, the assumptions of the 1-D formulation, i.e. predominantly unidirectional flow, hold well. The relative errors in flow and pressure were small between the 1-D and 3-D carotid models, with $\varepsilon_{P,\text{avg}}$ and $\varepsilon_{Q,\text{avg}}$ generally less than 0.3%, as shown in Fig. 3. In the baseline aorta case, however, the differences between the 1-D and 3-D models were greater (Fig. 4), particularly at the inlet, where the 3-D model shows a more pronounced systolic "shoulder" (at $t \approx 0.1$ s) in the pressure waveform compared to the 1-D model. Furthermore, the pressure gradient between the inlet and outlet is greater in the 3-D model during peak systole and also exhibits a phase-lag between the 1-D and 3-D models, i.e., the time at which the pressure gradient from the 3-D model reverses direction during systole is delayed compared to the 1-D model.

Inertial forces play a larger role in the aorta model compared to the carotid model, with the peak Reynolds number in the aorta model being nearly an order of magnitude greater than in the carotid model ($Re = 7, 140$ vs $Re = 748$). To investigate the impact of the Reynolds number in the pressure waveforms, we scaled down, by a factor of 9.54, the aorta model inflow to match the peak Reynolds number of the baseline carotid model. We observed that the average relative error in the pressure waveforms at the midpoint and outlet locations decreased, but the relative errors at the shoulder of the inlet pressure waveform and the phase lag in the pressure gradient were not reduced (Fig. 5).

To investigate the origin of these discrepancies further, we must reflect on the different treatments that our specific 1-D and 3-D implementations make regarding geometric nonlinearities. While both formulations consider equivalent linear material laws, the 3-D formulation assumes a linearized kinematics behavior for the vessel wall (i.e., a fixed computational grid is maintained throughout the simulation), whereas the 1-D formulation accounts for changes in cross-sectional area (see Eq. (7)). Therefore, the fixed-grid assumption of the 3-D formulation introduces errors in the velocity profile that are proportional in magnitude to the vessel wall strain. The aorta experiences both greater flow velocities and larger wall strains ($\varepsilon = r_{\max}/r_d$) compared to the carotid setting (i.e. $\varepsilon_{\text{aortic}} = 12.5\%$ versus $\varepsilon_{\text{carotid}} = 6\%$). These two phenomena are responsible for the larger

discrepancies between the 1-D and 3-D results during systole in the baseline aorta compared to the carotid example. This idea is supported by the larger diameter aorta model. Despite being a more compliant model than the baseline aorta (due to a larger cross-sectional area), it experiences smaller wall strains. The centerline velocities are also reduced compared to the baseline aorta model. We therefore have a situation where both the Reynolds number and the wall strains are reduced. This ultimately results in a smaller relative error in the shoulder of the inlet pressure waveform (Fig. 6) compared to the baseline aorta model (Fig. 4).

4.2. Impact of Tapering

The presence of tapering introduces errors between the 1-D and 3-D model in the systolic pressure (but not during the diastolic decay) in both carotid and aortic models (Figs. 7 and 8). The 3-D model more accurately captures the spatial changes in the velocity profile, and therefore, the viscous friction losses in the tapered tube. With tapering we observed greater errors between the 1-D and 3-D model in the pressure gradient between the inlet and outlet, as the 3-D model predicts that a greater pressure gradient is needed to drive flow during peak systole. In the tapered aorta case, inertial and frictional effects are naturally better captured in the 3-D model, resulting in greater errors in the pressure waveform than in the tapered carotid case.

4.3. Impact of Curvature

The velocity field in the curved 3-D domain is complex and not axisymmetric (Figs. 9 and 10). During systole, the region of higher velocity is located near the outer wall of the arch, and during deceleration, significant backflow occurs near the inner wall. As such, the 3-D model is inherently more accurate in capturing the inertial and frictional forces in the curved domain, which leads to differences in the integrated flow and pressure quantities compared to the 1-D model. Hence, we observed that the addition of a single plane of curvature slightly increased the relative errors in the pressure and flow waveforms (Fig. 9) compared to the uncurved baseline aorta case. In particular, the error in the systolic shoulder of the inlet pressure waveform was notably increased (compare Figs. 4 and 9).

External damping was necessary in the 3-D model to produce flow and pressure waves without spurious oscillations. This damping was not included in the 1-D formulation and contributes to some of the discrepancies observed. The added dissipation attenuated the high-frequency features of the flow and pressure waveforms in the 3-D model, whereas these features are more prominent in the 1-D model; i.e. the dicrotic notch and the early-diastolic flow reversal phase. We further observed that the addition of the second and third planes of curvature to the 3-D model did not further introduce significant differences between the 3-D and 1-D predictions (Fig. 10) compared to the single curvature case (Fig. 9). In Section 4.5 we investigate the relationship between external damping and curvature in the 3-D setting.

4.4. Bifurcation

The 1-D and 3-D model are in good agreement in the aortic bifurcation case. We observed small relative errors (average relative errors smaller than 2%) between the 1-D and 3-D

models (Fig. 11), which was expected considering the lower flow rate in comparison to the aorta case. Furthermore, changing the bifurcation angle from 47.9 degrees to 27.5 degrees resulted in a negligible change in the relative errors. A similar good agreement was obtained with a geometric model of the abdominal aorta featuring two 90 degree branches representing the renal arteries. These results suggest that the effect of energy losses at the aortic bifurcation on the pressure waveforms is minor, as was previously observed using *in-vitro* data [22].

4.5. Full Aorta Comparison

The full aorta model is essentially a combination of all the previously considered geometric features, including tapering, curvature, branching, and a variety of vessel diameters. As such, we expected to observe larger differences in the prediction of flow and pressure waveforms between the two theories. In general, the largest differences occur in systole, whereas the diastolic predictions are much closer. We can explain the closer agreement between models during diastole using a 0-D Windkessel model for pressure. Starting with the 1-D formulation, a space-independent Windkessel pressure, $p_w(t)$, can be derived by neglecting nonlinearities, flow inertia and viscous dissipation, and assuming that wall compliance and fluid peripheral resistance are the dominant effects [52]. Under these premises, $p_w(t)$ is given by

$$p_w = P_{out} + (p_w(T_0) - P_{out})e^{-\frac{t-T_0}{R_T C_T}} + \frac{e^{-\frac{t}{R_T C_T}}}{C_T} \int_{T_0}^{t} \left(Q_{in}(t') + \sum_{j=2}^{M} \frac{C^j R_1^j R_2^j}{R_2^j + R_1^j} \frac{dq_{out}^j(t')}{dt'} \right) e^{\frac{t'}{R_T C_T}} dt', \quad t \geq T_0, \quad (28)$$

where $Q_{in}(t)$ is the flow waveform at the inlet of the ascending aorta, $p_w(T_0)$ is the pressure p_w at $t = T_0$, T_0 is the time corresponding to the beginning of systole ($T_0 = 0$ in Fig. 14), $M - 1 < N$ is the number of terminal branches, and $q_{out}^j(t)$ is the outflow in the terminal Segment j. The net peripheral resistance (R_T) is given by Eq. (14), and the total arterial compliance (C_T) is given by Eq. (18). The parameters of the RCR Windkessel models are R_1, C, R_2 and P_{out} (Fig. 1). The validity of Eq. (28) is also supported by *in-vivo* studies, which show that the aortic pressure waveform is approximately uniform in space during approximately the last two thirds of diastole [60, 61].

Figure 14 (left) illustrates that the agreement between 3-D, 1-D and analytical pressures improves as diatole progresses, indicating that the physics of flow are fundamentally linear and inertia-free during this phase of the cardiac cycle. Conversely, systolic flow is fundamentally non-linear and advection/inertia dominated, and therefore larger differences between the two methods were observed.

The discrepancies observed in systole are partially due to the different treatment of the arterial wall mechanics in the two formulations: while both theories consider equivalent purely elastic material laws, the 3-D case requires a viscous dissipation term provided by the external tissue support model. Without this dissipation, the 3-D flow and pressure waveforms contain spurious, large amplitude high-frequency oscillations resulting from unconstrained rigid-body motion modes that are generated in non-axisymmetric flows. This

viscous damping, while necessary in the 3-D setting, attenuated the sharper features of the flow and pressure waveforms, most noticeably in the dicrotic notch and early-diastole flow reversal phases, compared to the predictions seen in the 1-D setting (Fig. 13).

It is worth noting that external tissue support can also be included in 1-D modeling, as recently demonstrated by [33]. That work focuses on the importance of including external tissue support in the 1-D formulation to reduce reflections at the 1-D/3-D interfaces. Furthermore, while the external tissue support will never be engaged in a 1-D setting to limit spurious wall motion as in the 3-D model, its presence will affect the deformation of the arterial wall due to the additional stiffness. Figure 14 (right) illustrates the impact of external tissue damping by introducing a new model consisting of a modified "straightened" full aorta geometry. We compared infrarenal flow and pressure waveforms in four different cases: 1) 3-D formulation in original full aorta geometry considering tissue damping; 2) 3-D fomulation in straightened full aorta geometry considering tissue damping; 3) 3-D formulation in straightened full aorta geometry without tissue damping; and 4) 1-D formulation. The results in the straightened 3-D aorta models (dashed blue and green lines) demonstrated sharper features than those observed in the 3-D curved aorta model (solid red lines) and, notwithstanding the larger pulse pressures in the 3-D model, resembled more closely the results from the 1-D model (dashed black lines). Furthermore, the exclusion of external tissue damping (green dashed lines) resulted in almost no difference in the pressure and flow waveforms in the straightened model. This behavior suggests that eliminating the aortic curvature reduced the rigid-body modes in the thoracic region and, even though the external viscous damping is still present, it is engaged to a lesser degree than in the original curved aorta model.

4.6. Limitations

It is important to note that the comparisons presented in this paper were between two particular implementations of 1-D and 3-D theories with equivalent boundary conditions and material laws. However, a one-to-one comparison of hemodynamics between the two theories is not always possible. A few examples of fundamental modeling differences that are not easy to overcome are: the inability to account for secondary flows and the assumption of a fixed velocity profile in the 1-D formulation; the linearized kinematics approach and the need for outflow boundary condition stabilization and external tissue support in the 3-D formulations.

To facilitate an improved comparison, the 1-D formulation could incorporate space- and time-varying velocity profiles [7, 56, 62, 63, 64]. Furthermore, external damping [9] and wall inertia [5] could be included in the 1-D model as well. On the other hand, the 3-D formulation would need to incorporate moving domains/meshes [11, 16] to enable a more consistent description of cross-sectional area changes between the two methods.

4.7. Implications of Fundamental Modeling Differences between 3-D and 1-D Theories

An inconsistency between our specific 1-D and 3-D implementations was introduced by assigning zero velocity boundary conditions at the inlet and outlet rings in the 3-D model, effectively clamping the vessels at those locations. Consequently, the conduit compliance

(C_c) of the vessels in the 3-D models is slightly reduced relative to the 1-D models; this becomes more significant as the length of the vessel domain decreases. The clamping has a negligible local effect on pressure and flow in the 3-D domain, even though the wall displacements near the inlets and outlets are reduced. A better treatment of the arterial wall boundary conditions in the 3-D formulation can be done using external tissue support formulations [39] and time-resolved medical-image data to inform both the radial and longitudinal components of the vessel wall motion. Lastly, an important inconsistency between our two modeling approaches is introduced by the need for external damping in the 3-D model in complex and curved geometries, such as the curved aorta and full aorta.

5. CONCLUSIONS

In this article, we have compared 1-D and 3-D hemodynamics in a series of idealized compliant arterial models of the carotid artery, thoracic aorta, aortic bifurcation and full aorta. The 1-D and 3-D formulations share common inflow and outflow boundary conditions and have equivalent material laws. We also presented an iterative algorithm to determine the parameters of each outflow boundary condition module to achieve desired systolic and diastolic pressures at a particular vessel. We have demonstrated good agreement between 1-D and 3-D predictions, especially during diastole. The larger differences in systole can be explained by the following: 1) the inability to account for secondary flow features, vessel curvature and a prescribed velocity profile shape in the 1-D model; and 2) the linearized treatment of the kinematics of the vessel wall and the external tissue support (which introduces viscous damping) in the 3-D model.

Our 1-D/3-D framework demonstrates the use of a 1-D model to determine boundary condition and material parameters that are subsequently fed to a corresponding 3-D model. Indeed, the relatively good agreement between the numerical predictions in the full aorta setting suggests that the 1-D model is a reasonable representation of the 3-D system in terms of the global behavior of the spatially-averaged pressure and flow waveforms. It follows that the 1-D model can be used to perform tasks such as 1) estimation of the parameters of outflow boundary conditions to reproduce clinical measurements and 2) sensitivity studies under different hemodynamic conditions to gain an understanding of the behavior of the arterial system. This overlapping 1-D/3-D approach will accelerate the selection of model parameters for 3-D subject-specific models.

Acknowledgments

References

1. Hughes T, Lubliner J. On the one-dimensional theory of blood flow in the larger vessels. Math Biosciences. 1973; 18:161–170.

2. Stergiopulos N, Young DF, Rogge TR. Computer simulation of arterial flow with applications to arterial and aortic stenoses. Journal of Biomechanics. Dec; 1992 25(12):1477–88. URL http://www.ncbi.nlm.nih.gov/pubmed/1491023. [PubMed: 1491023]

3. Reymond P, Bohraus Y, Perren F, Lazeyras F, Stergiopulos N. Validation of a Patient-Specific 1-D Model of the Systemic Arterial Tree. American Journal of Physiology Heart and Circulatory Physiology. May; 2011 301(May):H1173–H1182. URL http://www.ncbi.nlm.nih.gov/pubmed/21622820. 10.1152/ajpheart.00821.2010 [PubMed: 21622820]

4. Olufsen M, Peskin C, Kim W, Pedersen E, Nadim A, Larsen J. Numerical simulation and experimental validation of blood flow in arteries with structured-tree outflow conditions. Annals Biomed Eng. 2000; 28:1281–1299.

5. Formaggia L, Lamponi D, Quarteroni A. One-dimensional models for blood flow in arteries. J Eng Math. 2003; 47:251–276.

6. Sherwin SJ, Franke V, Peiro J, Parker KH. One-dimensional modelling of a vascular network in space-time variables. Journal of Engineering Mathematics. Dec; 2003 47(3):217–250. URL http://www.springerlink.com/openurl.asp?id=doi:10.1023/B:ENGI.0000007979.32871.e2http://www.springerlink.com/index/r33k14217n7130gt.pdf. 10.1023/B:ENGI.0000007979.32871.e2

7. Bessems D, Rutten M, van de Vosse F. A wave propagation model of blood flow in large vessels using an approximate velocity profile function. J Fluid Mech. 2007; 580:145–168.

8. Mynard J, Nithiarasu P. A 1D arterial blood flow model incorporating ventricular pressure, aortic valve and regional coronary flow using the locally conservative Galerkin (LCG) method. Commun Numer Meth Eng. 2008; 24:367–417.

9. Alastruey J, Khir AW, Matthys KS, Segers P, Sherwin SJ, Verdonck PR, Parker KH, Peiró J. Pulse wave propagation in a model human arterial network: Assessment of 1-D visco-elastic simulations against in vitro measurements. Journal of Biomechanics. Aug; 2011 44(12):2250–8. URL http://www.pubmedcentral.nih.gov/articlerender.fcgi?artid=3278302&tool=pmcentrez&rendertype=abstract. 10.1016/j.jbiomech.2011.05.041 [PubMed: 21724188]

10. Müller, L.; Toro, E. Well balanced high order solver for blood flow in networks of vessels with variable properties. International Journal for Numerical. 2013; http://onlinelibrary.wiley.com/doi/10.1002/cnm.2580/full

11. Perktold K, Rappitsch G. Computer simulation of local blood flow and vessel mechanics in a compliant carotid artery bifurcation model. Journal of Biomechanics. Jul; 1995 28(7):845–56. URL http://www.ncbi.nlm.nih.gov/pubmed/7657682. [PubMed: 7657682]

12. Taylor CA, Hughes TJR, Zarins CK. Finite element modeling of blood flow in arteries. Computer Methods in Applied Mechanics and Engineering. 1998; 7825(97) http://www.sciencedirect.com/science/article/pii/S004578259880008X.

13. Quarteroni A, Tuveri M, Veneziani A. Computational vascular fluid dynamics: problems, models and methods. Computing and Visualization in Science. Mar.2000 2:163–97.

14. Steinman D, Milner J, Norley C, Lownie S, Holdsworth D. Image-based computational simulation of flow dynamics in a giant intracranial aneurysm. American Journal of Neuroradiology. Apr; 2003 24(4):559–566. [PubMed: 12695182] 4th World Congress of Biomechanics; Calgary, Canada. Aug, 2002;

15. Cebral J, Castro M, Burgess J, Pergolizzi R, Sheridan M, Putman C. Characterization of cerebral aneurysms for assessing risk of rupture by using patient-specific computational hemodynamics models. American Journal of Neuroradiology. Nov-Dec;2005 26(10):2550–2559. [PubMed: 16286400]

16. Gerbeau JF, Vidrascu M, Frey P. Fluid-structure interaction in blood flows on geometries based on medical imaging. Computers & Structures. Jan; 2005 83(2–3):155–165. URL http://linkinghub.elsevier.com/retrieve/pii/S0045794904003001. 10.1016/j.compstruc.2004.03.083

17. Figueroa CA, Vignon-Clementel IE, Jansen KE, Hughes TJR, Taylor CA. A coupled momentum method for modeling blood flow in three-dimensional deformable arteries. Computer Methods in Applied Mechanics and Engineering. Aug; 2006 195(41–43):5685–5706. URL http://linkinghub.elsevier.com/retrieve/pii/S004578250500513X. 10.1016/j.cma.2005.11.011

18. van de Vosse F, Stergiopulos N. Pulse wave propagation in the arterial tree. Annu Rev Fluid Mech. 2011; 43:467–499.

19. Alastruey, J.; Parker, K.; Sherwin, S. Arterial pulse wave haemodynamics. Proc. BHR Group's 11th International Conference on Pressure Surges; Lisbon, Portugal. 24th – 26th October; 2012. p. 401-442.

20. Parker K. An introduction to wave intensity analysis. Med Bio Eng Comput. 2009; 47:175–188. [PubMed: 19205773]

21. Steele B, Wan J, Ku J, Hughes T, Taylor C. In vivo validation of a one-dimensional finite-element method for predicting blood flow in cardiovascular bypass grafts. Ieee Transactions On Biomedical Engineering. Jun; 2003 50(6):649–656.10.1109/TBME.2003.812201 [PubMed: 12814231]

22. Matthys KS, Alastruey J, Peiro J, Khir AW, Segers P, Verdonck PR, Parker KH, Sherwin SJ. Pulse wave propagation in a model human arterial network: Assessment of 1-D numerical simulations against in vitro measurements. Journal Of Biomechanics. 2007; 40(15):3476–3486.10.1016/j.jbiomech.2007.05.027 [PubMed: 17640653]

23. Humphrey J, Strumpf R, Yin F. Determination of a constitutive relation for passive myocardium. 2. Parameter-estimation. Journal of Biomechanical Engineering - Transactions of the ASME. Aug; 1990 112(3):340–346.10.1115/1.2891194

24. Xiong G, Figueroa CA, Xiao N, Taylor CA. Simulation of blood flow in deformable vessels using subject-specific geometry and spatially varying wall properties. International Journal for Numerical Methods in Biomedical Engineering. Jul; 2011 27(7):1000–1016.10.1002/cnm.1404 [PubMed: 21765984]

25. Prasad A, Xiao N, Gong XY, Zarins C, Figueroa CA. A computational framework for investigating the positional stability of aortic endografts. Biomechanics and Modeling in Mechanogiology. 10.1007/s10237-012-0450-3

26. Taylor CA, Figueroa CA. Patient-specific modeling of cardiovascular mechanics. Annual Review of Biomedical Engineering. Jan; 2009 11(April):109–34. URL http://www.ncbi.nlm.nih.gov/pubmed/19400706. 10.1146/annurev.bioeng.10.061807.160521

27. Moore S, Moorhead K, Chase J, David T, Fink J. One-dimensional and three-dimensional models of cerebrovascular flow. Journal Of Biomechanical Engineering-transactions Of The Asme. Jun; 2005 127(3):440–449.10.1115/1.1894350

28. Grinberg L, Cheever E, Anor T, Madsen JR, Karniadakis GE. Modeling blood flow circulation in intracranial arterial networks: a comparative 3D/1D Simulation Study. Annals Of Biomedical Engineering. Jan; 2011 39(1):297–309.10.1007/s10439-010-0132-1 [PubMed: 20661645]

29. Reymond P, Perren F, Lazeyras F, Stergiopulos N. Patient-specific mean pressure drop in the systemic arterial tree, a comparison between 1-D and 3-D models. Journal of Biomechanics. Aug. 2012 45:2499–2505. URL http://linkinghub.elsevier.com/retrieve/pii/S0021929012004174. 10.1016/j.jbiomech.2012.07.020 [PubMed: 22884968]

30. Xiao N, Humphrey JD, Figueroa CA. Multi-scale computational model of three-dimensional hemodynamics within a deformable full-body arterial network. Journal of Computational Physics. 10.1016/j.jcp.2012.09.016

31. Passerini T, de Luca M, Formaggia L, Quarteroni A, Veneziani A. A 3D/1D geometrical multiscale model of cerebral vasculature. Journal of Engineering Mathematics. Aug; 2009 64(4): 319–330.10.1007/s10665-009-9281-3

32. van de Vosse, FN.; Stergiopulos, N. Pulse Wave Propagation in the Arterial Tree. In: Davis, SH.; Moin, P., editors. Annual Review of Fluid Mechanics. Vol. 43. 2011. p. 467-499.

33. Formaggia, L.; Quarteroni, A.; Vergara, C. On the physical consistency between three-dimensional and one-dimensional models in haemodynamics. Journal of Computational Physics. 2012. http://www.sciencedirect.com/science/article/pii/S0021999112004342

34. Peiró, J.; Veneziani, A. Reduced models of the cardiovascular system. In: Formaggia, L.; Quarteroni, A.; Veneziani, A., editors. Cardiovascular Mathematics Modeling and Simulation of the Circulatory System. Springer-Verlag; Milano: 2009. p. 347-394.

35. Smith NP, Pullan AJ, Hunter PJ. An anatomically based model of transient coronary blood flow in the heart. SIAM Journal on Applied Mathematics. Jan; 2002 62(3):990–1018. URL http://epubs.siam.org/doi/abs/10.1137/S0036139999355199. 10.1137/S0036139999355199

36. ani S, Kim E. Mathematical analysis of the quasilinear effects in a hyperbolic model of blood flow through compliant axi-symmetric vessels. Math Meth Appl Sci. 2003; 26:1161–1186.

37. Quarteroni, A.; Formaggia, L. Mathematical modelling and numerical simulation of the cardiovascular system. In: Ayache, N., editor. Modelling of Living Systems. Elsevier; Amsterdam: 2004.

38. Alastruey J, Parker KH, Peiró J, Sherwin SJ. Lumped parameter outflow models for 1-D blood flow simulations: effect on pulse waves and parameter estimation. Communications in Computational Physics. 2008; 4:317–336. URL http://www.bg.ic.ac.uk/research/j.alastruey-arimon/Figs/TerminalBCs.pdf.

39. Moireau, P.; Xiao, N.; Astorino, M.; Figueroa, CA.; Chapelle, D.; Taylor, CA.; Gerbeau, JF. External tissue support and fluid-structure simulation in blood flows. Biomechanics and Modeling in Mechanobiology. Feb. 2011 http://www.ncbi.nlm.nih.gov/pubmed/21308393

40. Vignon-Clementel IE, Figueroa CA, Jansen KE, Taylor CA. Outflow boundary conditions for three-dimensional finite element modeling of blood flow and pressure in arteries. Computer Methods in Applied Mechanics and Engineering. Jun; 2006 195(29–32):3776–3796. URL http://linkinghub.elsevier.com/retrieve/pii/S0045782505002586. 10.1016/j.cma.2005.04.014

41. Vignon-Clementel IE, Figueroa CA, Jansen KE, Taylor CA. Outflow boundary conditions for 3D simulations of non-periodic blood flow and pressure fields in deformable arteries. Computer Methods in Biomechanics and Biomedical engineering. Oct; 2010 13(5):625–40. URL http://www.ncbi.nlm.nih.gov/pubmed/20140798. 10.1080/10255840903413565 [PubMed: 20140798]

42. Kim HJ, Figueroa CA, Hughes TJR, Jansen KE, Taylor CA. Augmented Lagrangian method for constraining the shape of velocity profiles at outlet boundaries for three-dimensional finite element simulations of blood flow. Computer Methods in Applied Mechanics and Engineering. Sep; 2009 198(45–46):3551–3566. URL http://linkinghub.elsevier.com/retrieve/pii/S0045782509000887. 10.1016/j.cma.2009.02.012

43. Brooks AN, Hughes TJR. Streamline upwind/Petrov-Galerkin formulations for convection dominated flows with particular emphasis on the incompressible Navier-Stokes equations. Computer Methods in Applied Mechanics and Engineering. 1982; 32(1–3):199–259. URL http://www.sciencedirect.com/science/article/pii/0045782582900718. 10.1016/0045-7825(82)90071-8

44. Franca LP, Frey SL. Stabilized finite element methods: II. The incompressible Navier-Stokes equations. Computer Methods in Applied Mechanics and Engineering. Sep; 1992 99(2–3):209–233. URL http://linkinghub.elsevier.com/retrieve/pii/004578259290041H. 10.1016/0045-7825(92)90041-H

45. Whiting CH, Jansen KE. A stabilized finite element method for the incompressible Navier-Stokes equations using a hierarchical basis. International Journal for Numerical Methods in Fluids. Jan; 2001 35(1):93–116. URL http://doi.wiley.com/10.1002/1097-0363%2820010115%2935%3A1%3C93%3A%3AAID-FLD85%3E3.0.CO%3B2-G. 10.1002/1097-0363(20010115)35:1⟨93::AID-FLD85⟩3.0.CO;2-G

46. Chung J, Hulbert GM. A time integration algorithm for structural dynamics with improved numerical dissipation: the generalized-alpha method. Journal of Applied Mechanics. 1993; 6(June):371–375. URL http://scholar.google.com/scholar?hl=en&btnG=Search&q=intitle:A+Time+Integration+Algorithm+for+Structural+Dynamics+With+Improved+Numerical+Dissipation:+The+Generalized-+Method#0.

47. Jansen KE, Whiting CH, Hulbert GM. A generalized-α method for integrating the filtered Navier–Stokes equations with a stabilized finite element method. Computer Methods in Applied Mechanics and Engineering. Apr; 2001 190(31):305–319. URL http://linkinghub.elsevier.com/retrieve/pii/S0045782500002036. 10.1016/S0045-7825(00)00203-6

48. Figueroa CA, Baek S, Taylor CA, Humphrey JD. A computational framework for fluid-solid-growth modeling in cardiovascular simulations. Computer Methods in Applied Mechanics and

Engineering. Sep; 2009 198(45–46):3583–3602. URL http://www.pubmedcentral.nih.gov/articlerender.fcgi?artid=2770883&tool=pmcentrez&rendertype=abstract. 10.1016/j.cma.2008.09.013 [PubMed: 20160923]

49. Baek S, Gleason RL, Rajagopal KR, Humphrey JD. Theory of small on large: Potential utility in computations of fluid–solid interactions in arteries. Computer Methods in Applied Mechanics and Engineering. Jun; 2007 196(31–32):3070–3078. URL http://linkinghub.elsevier.com/retrieve/pii/S0045782507000424. 10.1016/j.cma.2006.06.018

50. Alastruey J, Passerini T, Formaggia L, Peiró J. Physical determining factors of the arterial pulse waveform: theoretical analysis and calculation using the 1-D formulation. Journal of Engineering Mathematics. Sep; 2012 77(1):19–37. URL http://www.springerlink.com/index/10.1007/s10665-012-9555-z. 10.1007/s10665-012-9555-z

51. Simon AC, Safar ME, Levenson JA, London GM, Levy BI, Chau NP. An evaluation of large arteries compliance in man. American Journal of Physiology Heart and Circulatory Physiology. 1979; 237(5):H550–H554. URL http://ajpheart.physiology.org/content/237/5/H550.short.

52. Alastruey J, Parker KH, Peiró J, Sherwin SJ. Analysing the pattern of pulse waves in arterial networks: a time-domain study. Journal of Engineering Mathematics. Feb; 2009 64(4):331–351. URL http://www.springerlink.com/index/10.1007/s10665-009-9275-1. 10.1007/s10665-009-9275-1

53. Spilker RL, Taylor CA. Tuning multidomain hemodynamic simulations to match physiological measurements. Annals Of Biomedical Engineering. Aug; 2010 38(8):2635–2648.10.1007/s10439-010-0011-9 [PubMed: 20352338]

54. Devault K, Gremaud PA, Novak V, Olufsen MS, Vernieres G, Zhao P. Blood flow in the circle of Willis: modeling and calibration. Multiscale Modeling & Simulation. 2008; 7(2):888–909.10.1137/07070231X [PubMed: 19043621]

55. Nichols, WW.; O'Rourke, MF. McDonald's Blood Flow in Arteries: Theoretical, Experimental, and Clinical Principles. Vol. 11. Hodder Arnold: Distributed in the United States of America by Oxford University Press; 1998.

56. Reymond P, Merenda F, Perren F, Rüfenacht D, Stergiopulos N. Validation of a one-dimensional model of the systemic arterial tree. American Journal of Physiology Heart and Circulatory Physiology. Jul; 2009 297(1):H208–H222. URL http://www.ncbi.nlm.nih.gov/pubmed/19429832. 10.1152/ajpheart.00037.2009 [PubMed: 19429832]

57. Yearwood TL, Chandran KB. Experimental investigation of steady flow through a model of the human aortic arch. Journal of Biomechanics. Jan; 1980 13(12):1075–88. URL http://www.ncbi.nlm.nih.gov/pubmed/7204423. [PubMed: 7204423]

58. Sun H, Kuban BD, Schmalbrock P, Friedman MH. Measurement of the geometric parameters of the aortic bifurcation from magnetic resonance images. Annals of Biomedical Engineering. 1994; 22(3):229–39. URL http://www.ncbi.nlm.nih.gov/pubmed/7978544. [PubMed: 7978544]

59. Shin IY, Chung YG, Shin WH, Im SB, Hwang SC, Kim BT. A morphometric study on cadaveric aortic arch and its major branches in 25 Korean adults: the perspective of endovascular surgery. Journal of Korean Neurosurgical Society. Aug; 2008 44(2):78–83. URL http://www.pubmedcentral.nih.gov/articlerender.fcgi?artid=2588331&tool=pmcentrez&rendertype=abstract. 10.3340/jkns.2008.44.2.78 [PubMed: 19096697]

60. Wang JJ, O'Brien A, Shrive N, Parker K, Tyberg J. Time-domain representation of ventricular-arterial coupling as a windkessel and wave system. Am J Physiol Heart Circ Physiol. 2003; 284:H1358–H1368. [PubMed: 12531729]

61. Aguado-Sierra J, Alastruey J, Wang JJ, Hadjiloizou N, Davies J, Parker K. Separation of the reservoir and wave pressure and velocity from measurements at an arbitrary location in arteries. Proc Inst Mech Eng, Part H, J Eng Med. 2008; 222:403–416.

62. ani S, Lamponi D, Mikeli A, Tamba a J. Self-consistent effective equations modeling blood flow in medium- to-large compliant arteries. Multiscale Mod Sim. 2005; 3:559–596.

63. Robertson A, Sequeira A. A director theory approach for modeling blood flow in the arterial system: An alternative to classical 1D models. Mathem Mod and Meth App Sci. 2005; 15:871–906.

64. Azer K, Peskin C. A one-dimensional model of blood flow in arteries with friction and convection based on the Womersley velocity profile. Cardiov Eng. 2007; 7:51–73.

65. Riley W, Barnes R, Evans G, Burke G. Ultrasonic measurement of the elastic modulus of the common carotid artery. The Atherosclerosis Risk in Communities (ARIC) Study. Stroke. Jul; 1992 23(7):952–956. URL http://stroke.ahajournals.org/cgi/doi/10.1161/01.STR.23.7.952. 10.1161/01.STR.23.7.952 [PubMed: 1615543]

66. Cheng C, Herfkens RJ, Taylor CA. Abdominal aortic hemodynamic conditions in healthy subjects aged 50–70 at rest and during lower limb exercise: in vivo quantification using MRI. Atherosclerosis. Jun; 2003 168(2):323–331. URL http://linkinghub.elsevier.com/retrieve/pii/S0021915003000996. 10.1016/S0021-9150(03)00099-6 [PubMed: 12801616]
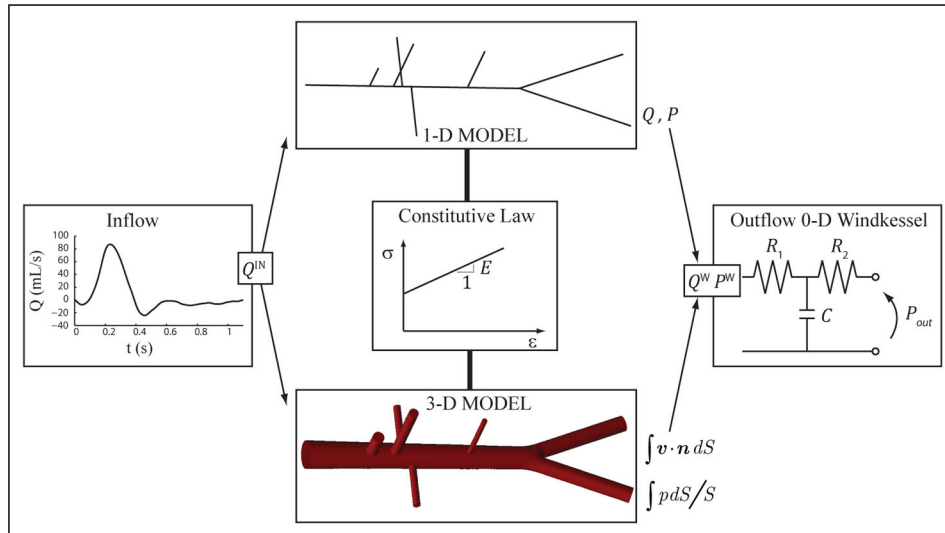
Figure 1.
Schematic representation of the modeling approach adopted in this study: 1-D and 3-D models share common inflow and outflow boundary conditions, as well as compatible consitutive laws. The 1-D geometry is obtained from the centerlines of the 3-D model, and vessel diameters and wall thickness are identical.
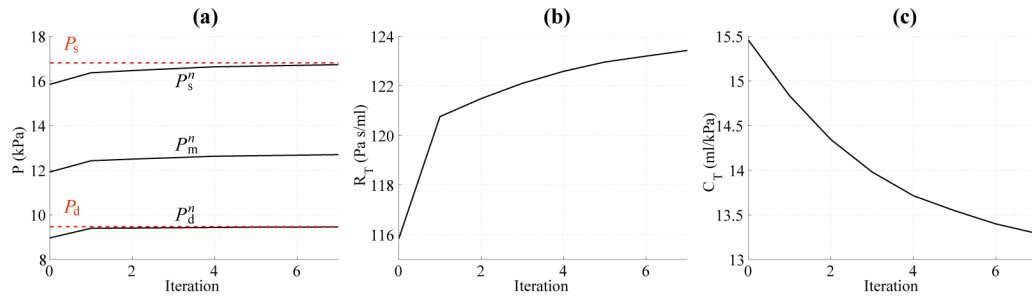
Figure 2.
(a) Evolution of systolic (P_s^n), mean (P_m^n) and diastolic (P_d^n) pressure, (b) net peripheral resistance (R_T), and (c) total compliance C_T with the iteration number (n) for the baseline aorta. The target systolic (P_s) an diastolic (P_d) pressures are shown in red dashed lines.
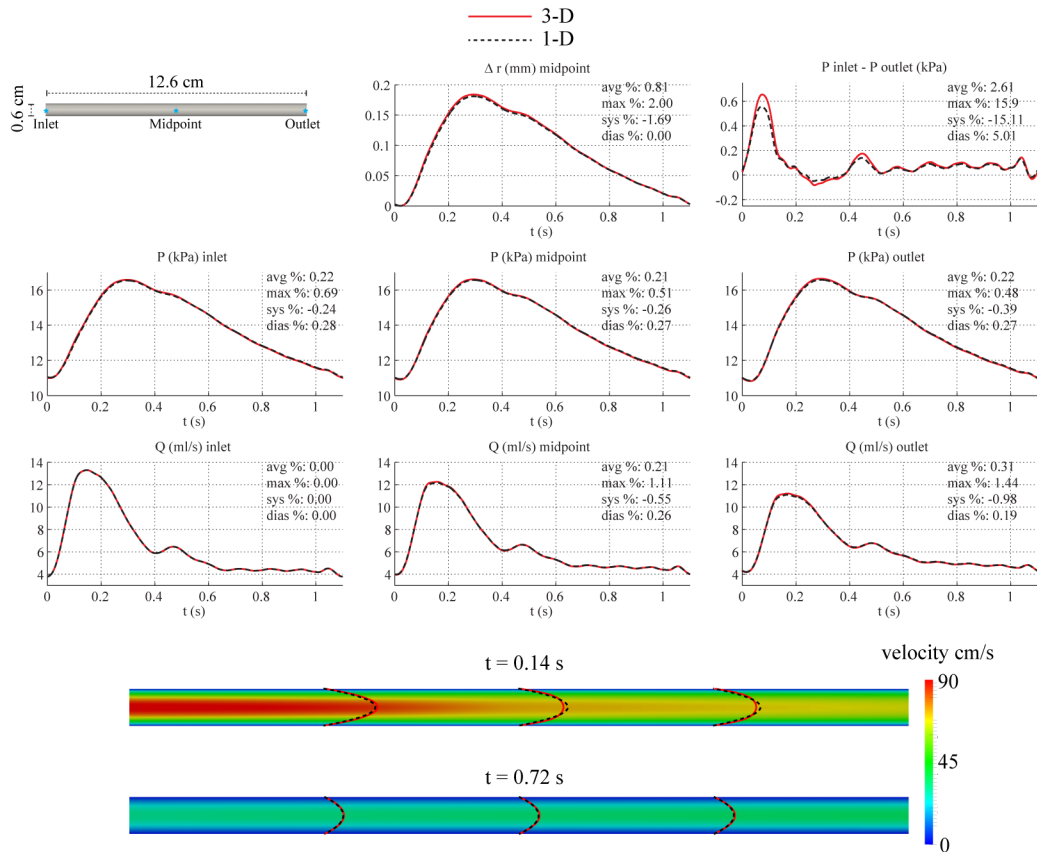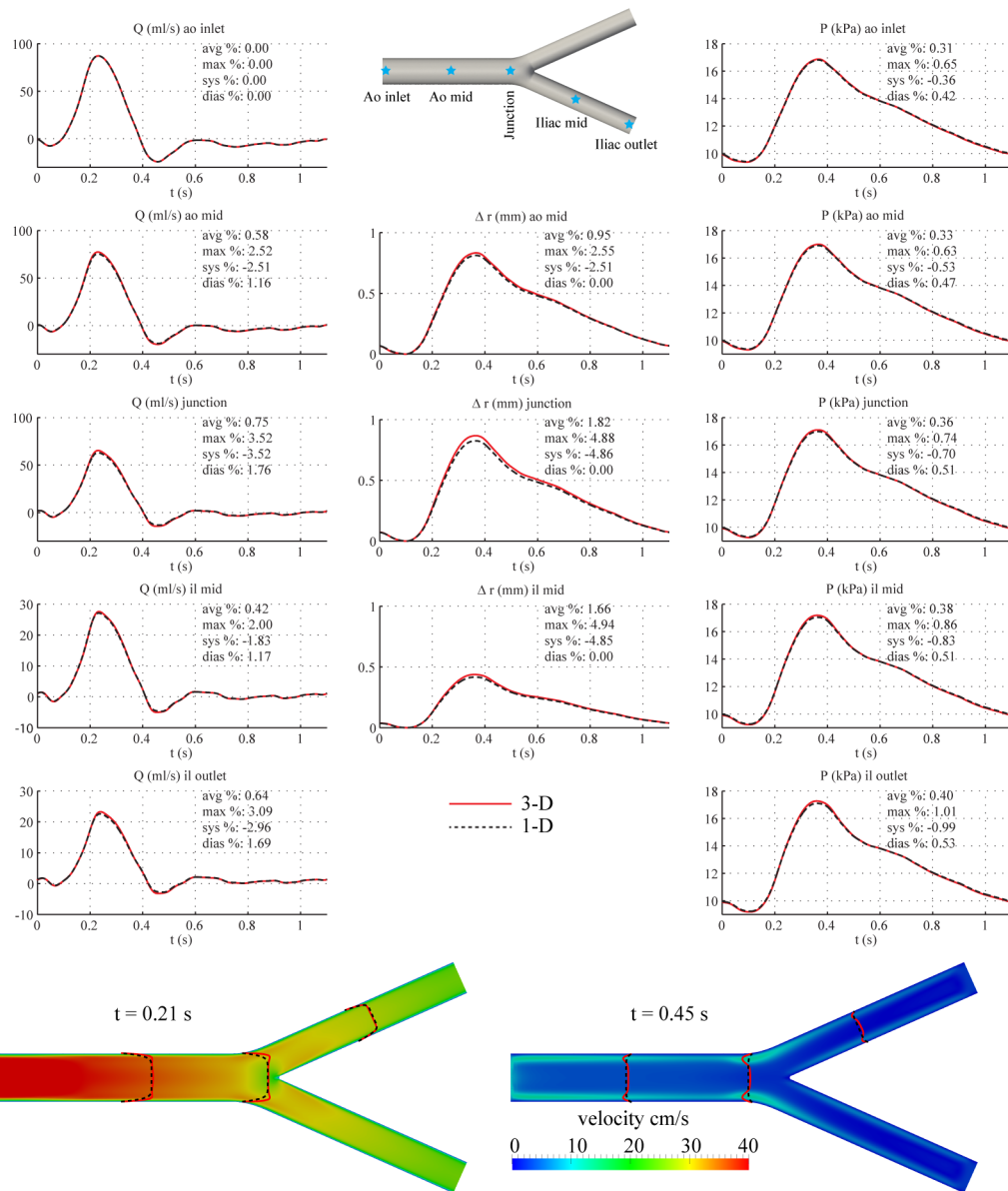
Figure 3.

Baseline common carotid case. Top: flow rate and pressure with time at the inlet, midpoint and outlet, radius with time at the midpoint, and pressure gradient between inlet and outlet in the 3-D model (solid lines) and 1-D model (dashed lines) with relative error metrics (Section 2.6). Bottom: velocity magnitude in the reference domain of the 3-D model (colormap). Velocity profiles of the 3-D model (solid lines, axial velocity component) and the 1-D model (dashed lines) at three locations and two time points.
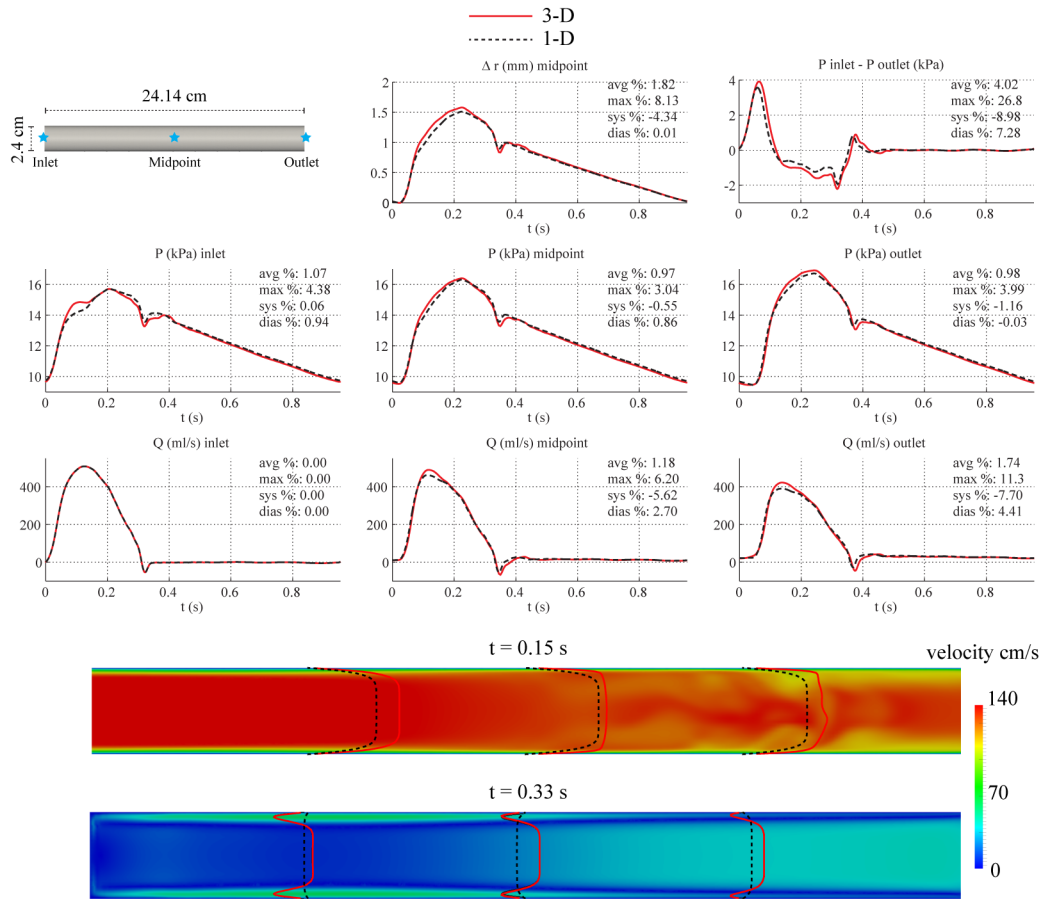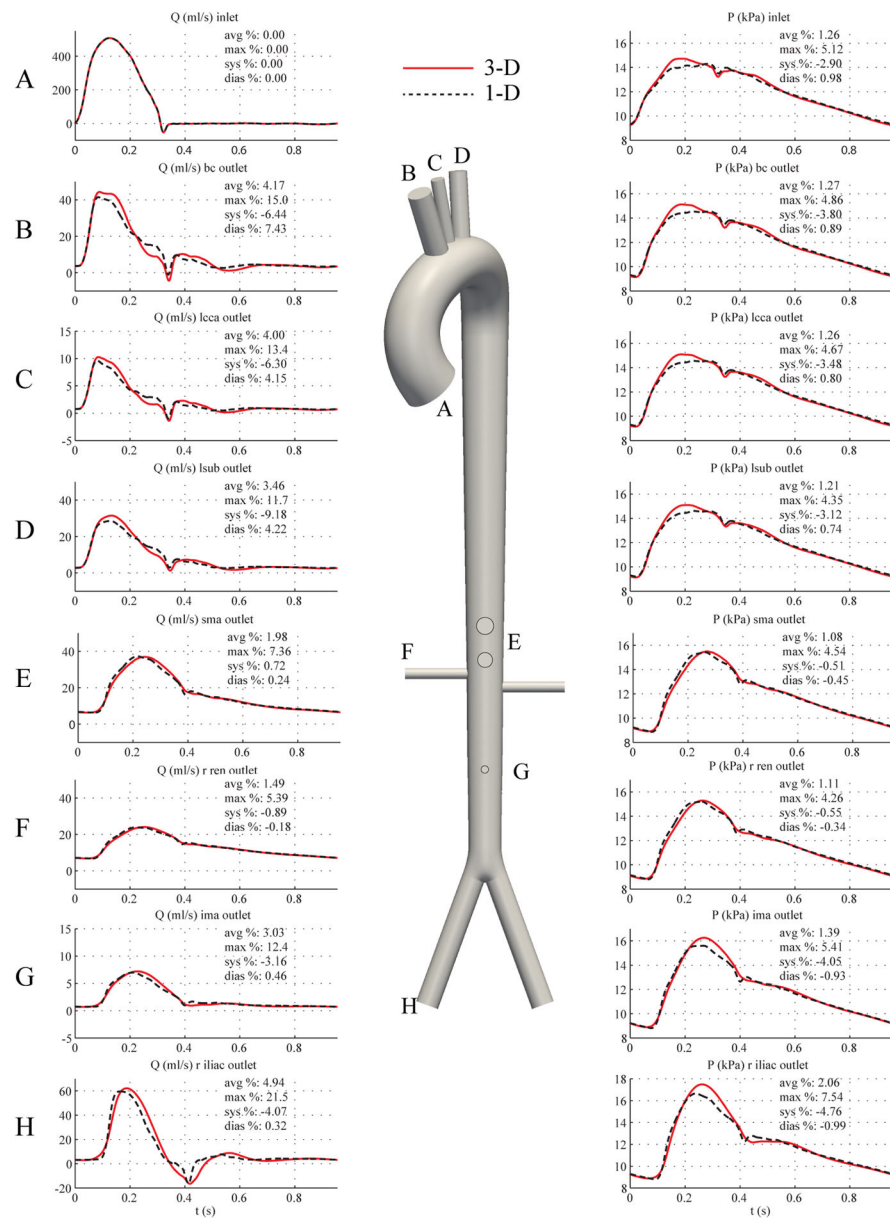
Figure 4.
Baseline aorta case. Top: flow rate and pressure with time at the inlet, midpoint and outlet, radius with time at the midpoint, and pressure gradient between inlet and outlet in the 3-D model (solid lines) and 1-D model (dashed lines) with relative error metrics (Section 2.6). Bottom: velocity magnitude in the reference domain of the 3-D model (colormap). Velocity profiles of the 3-D model (solid lines, axial velocity component) and the 1-D model (dashed lines) at three locations and two time points.
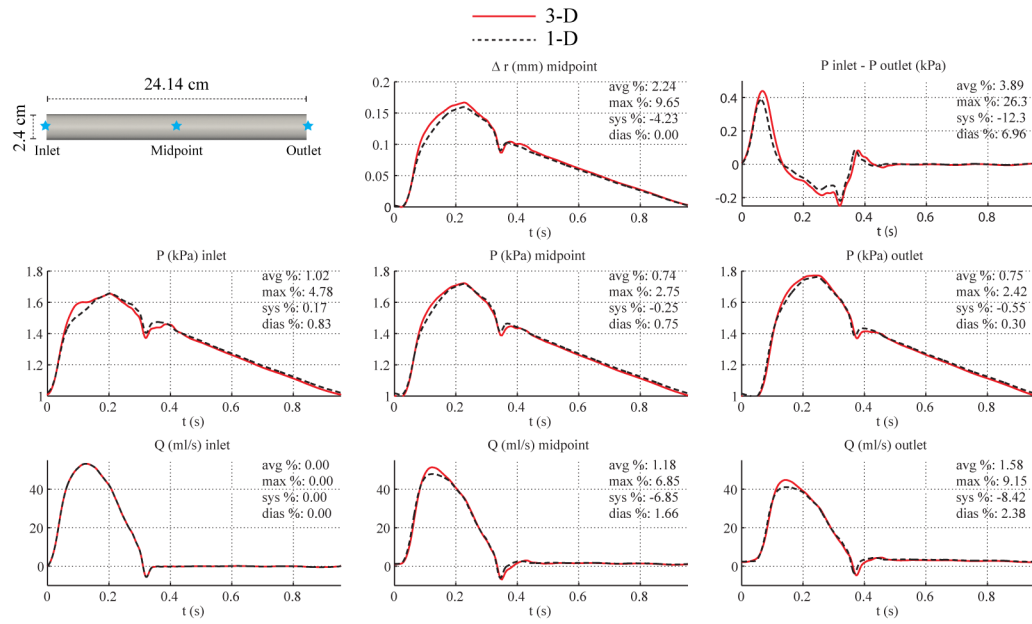
Figure 5.
Low-flow aorta case. Top: flow rate and pressure with time at the inlet, midpoint and outlet, radius with time at the midpoint, and the pressure gradient between inlet and outlet in the 3-D model (solid lines) and 1-D model (dashed lines) with relative error metrics (Section 2.6).
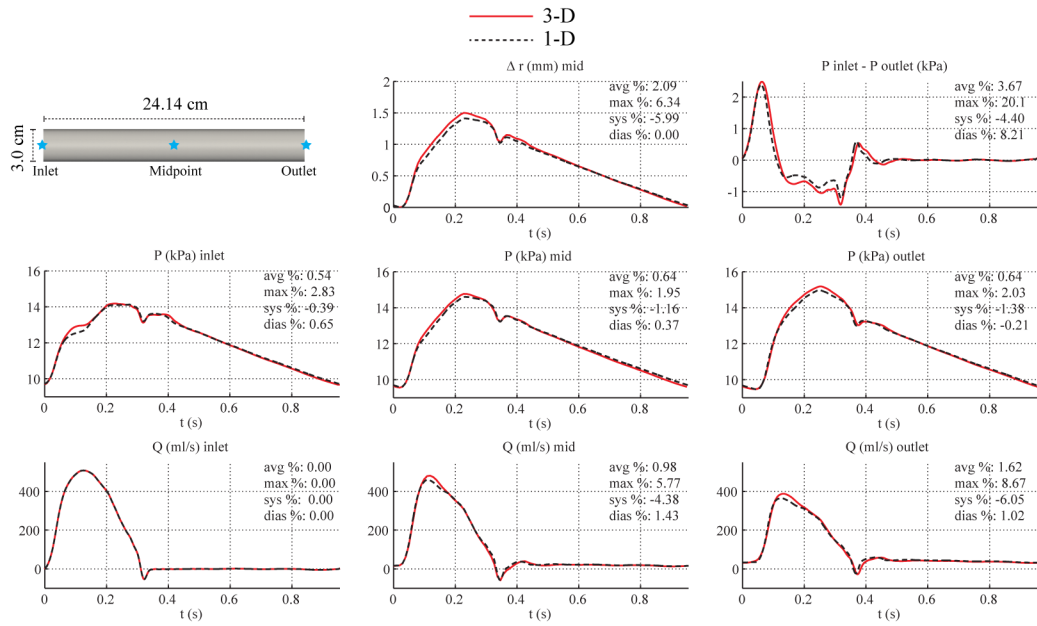
Figure 6.
Larger-diameter aorta case. Top: flow rate and pressure with time at the inlet, midpoint and outlet, radius with time at the midpoint, and pressure gradient between inlet and outlet in the 3-D model (solid lines) and 1-D model (dashed lines) with relative error metrics (Section 2.6).
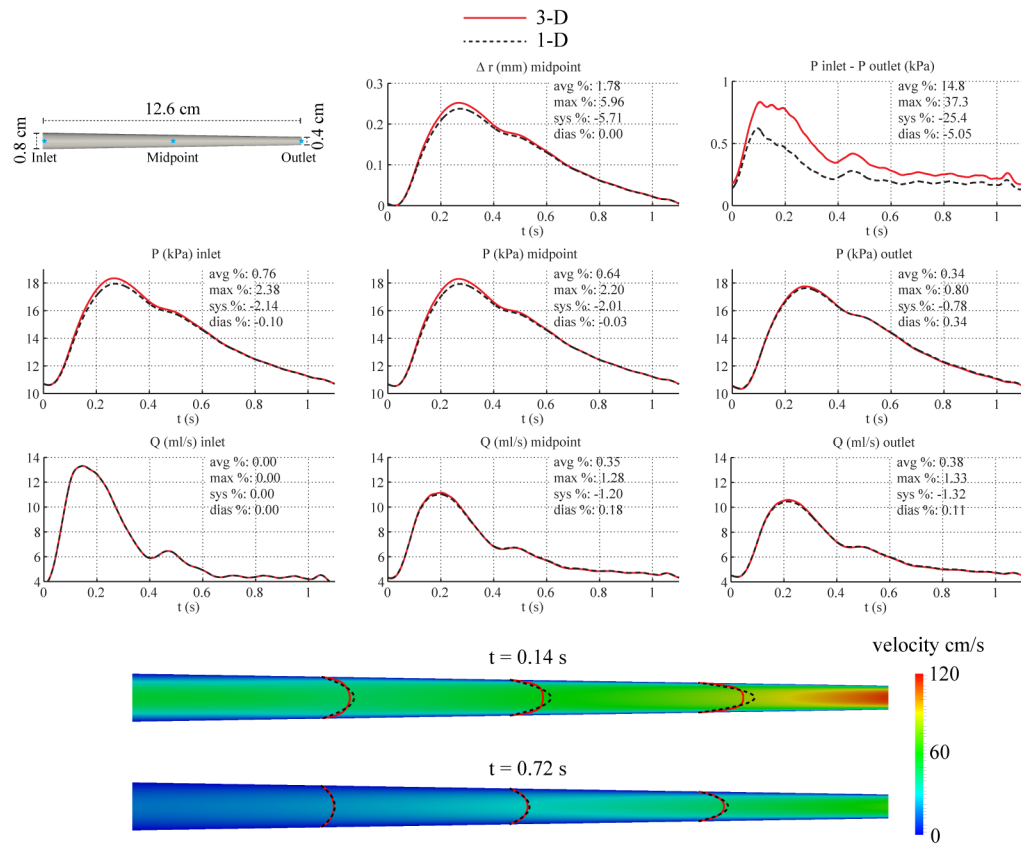
Figure 7.
Tapered carotid case. Top: flow rate and pressure with time at the inlet, midpoint and outlet, radius with time at the midpoint, and pressure gradient between inlet and outlet in the 3-D model (solid lines) and 1-D model (dashed lines) with relative error metrics (Section 2.6). Bottom: velocity magnitude in the reference domain of the 3-D model (colormap). Velocity profiles of the 3-D model (solid lines, axial velocity component) and the 1-D model (dashed lines) at three locations and two time points.
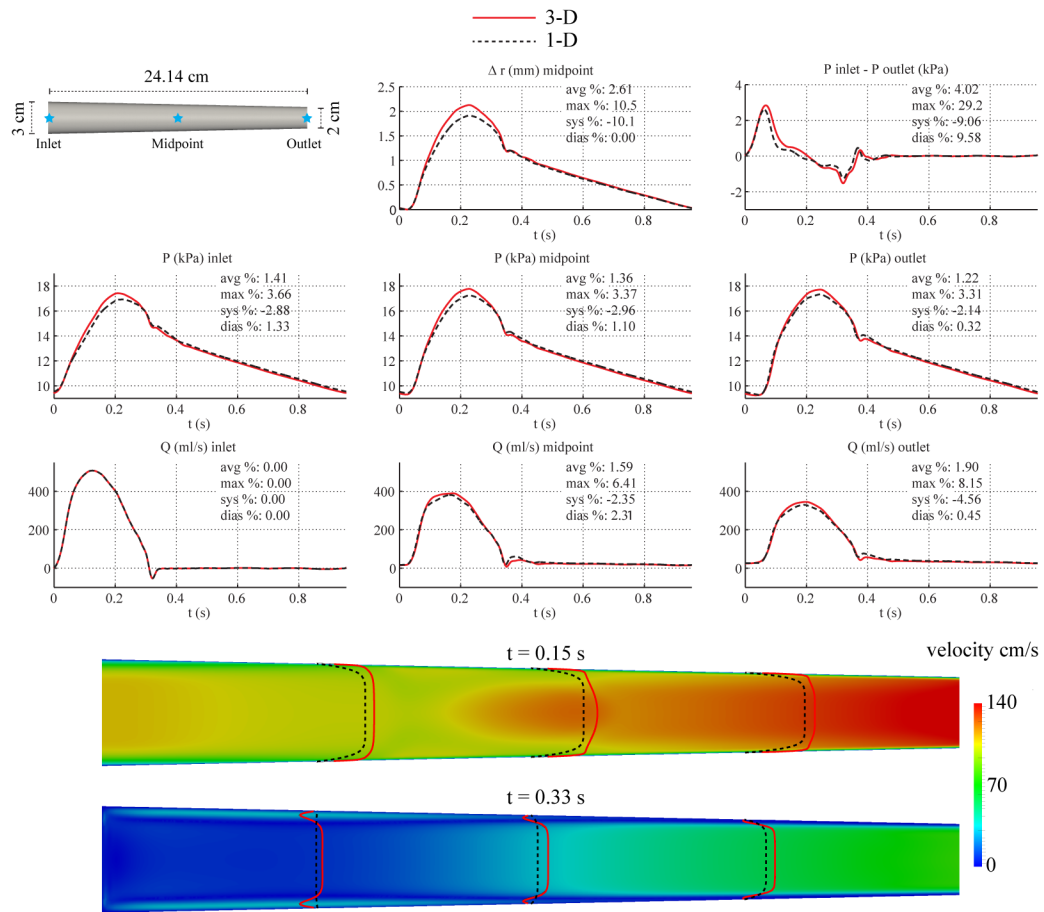
Figure 8.
Tapered aorta case. Top: flow rate and pressure with time at the inlet, midpoint and outlet, radius with time at the midpoint, and pressure gradient between inlet and outlet in the 3-D model (solid lines) and 1-D model (dashed lines) with relative error metrics (Section 2.6). Bottom: velocity magnitude in the reference domain of the 3-D model (colormap). Velocity profiles of the 3-D model (solid lines, axial velocity component) and the 1-D model (dashed lines) at three locations and two time points.
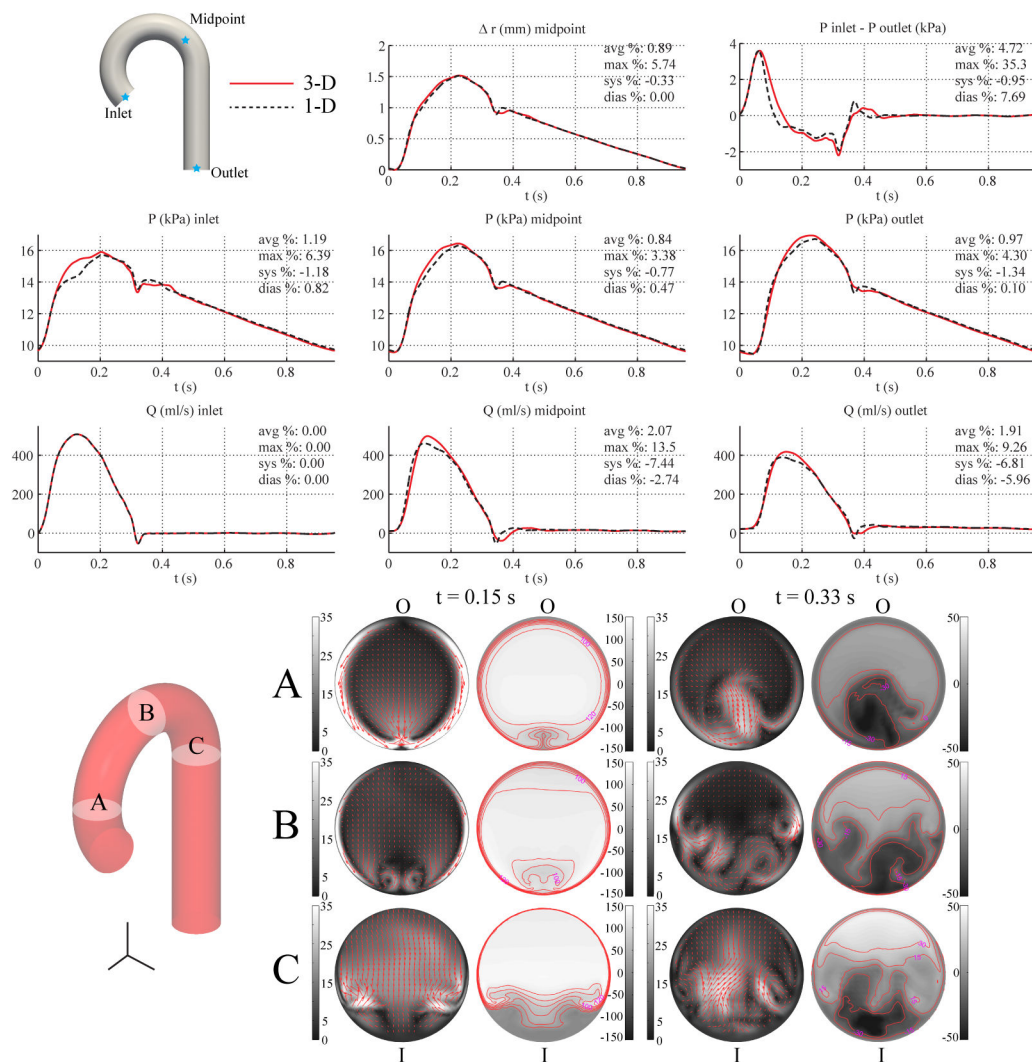
Figure 9.
Single-curvature aorta case. Top: flow rate and pressure with time at the inlet, midpoint and outlet, radius with time at the midpoint, and pressure gradient between inlet and outlet in the 3-D model (solid lines) and 1-D model (dashed lines) with relative error metrics (Section 2.6). Bottom: in-plane (colormap and arrows, left) velocity and out-of-plane (colormap, right) components of the velocity field in the 3-D model at three cross-sections. Velocities are given in cm/s. The outer and inner curvatures are labeled as "O" and "I", respectively.
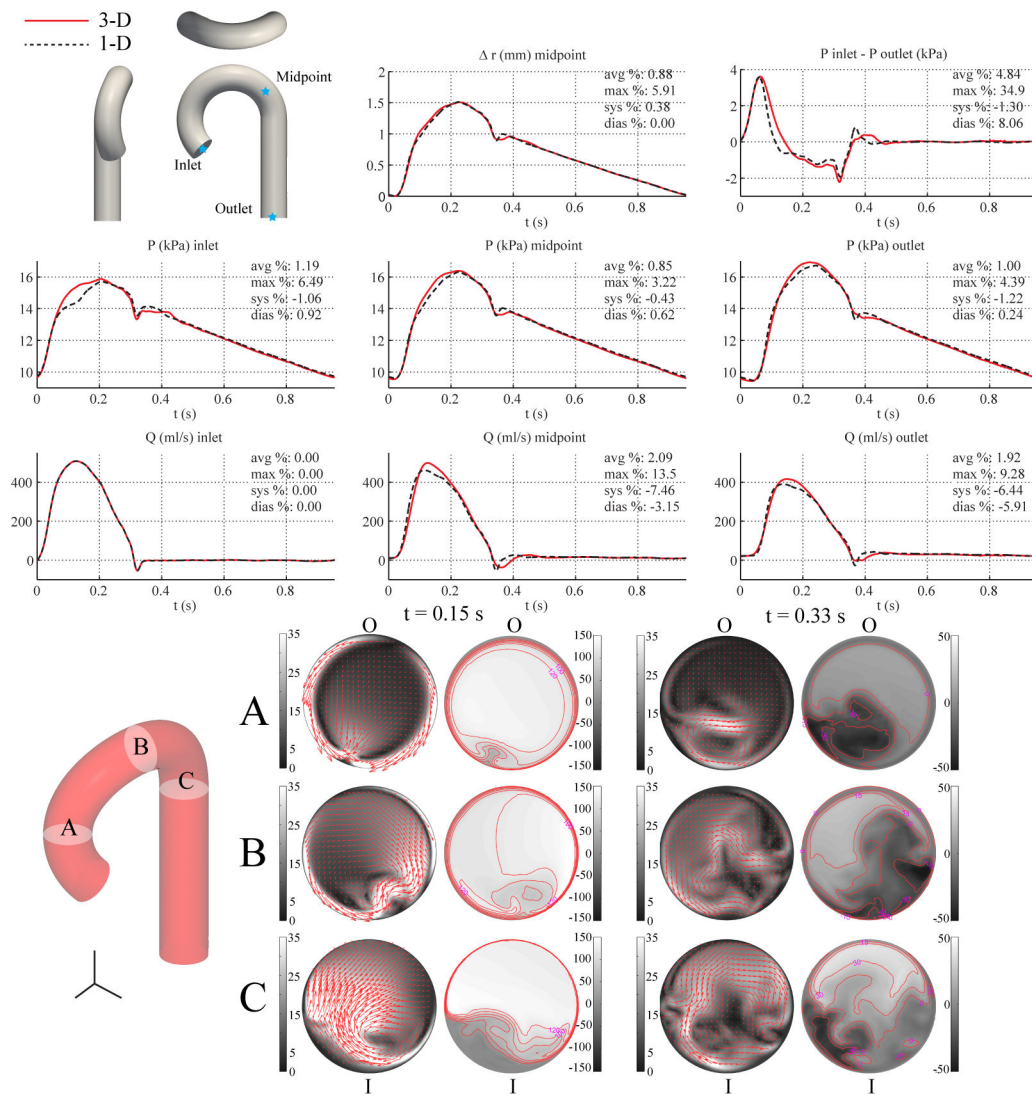
Figure 10.
Multiple-curvature aorta case. Top: flow rate and pressure with time at the inlet, midpoint and outlet, radius with time at the midpoint, and the pressure gradient between inlet and outlet in the 3-D model (solid lines) and 1-D model (dashed lines) with relative error metrics (Section 2.6). Bottom: in-plane (colormap and arrows, left) velocity and out-of-plane (colormap, right) components of the velocity field in the 3-D model at three cross-sections. Velocities are given in cm/s. The outer and inner curvatures are labeled as "O" and "I", respectively.

Figure 11.
Aortic bifurcation case. Top: flow rate, pressure, change in radius with time at several locations and pressure gradient between inlet and outlet in the 3-D model (solid lines) and 1-D model (dashed lines) with relative error metrics (Section 2.6). Bottom: velocity magnitude in the reference domain of the 3-D model (colormap). Velocity profiles of the 3-D model (solid lines, axial velocity component) and the 1-D model (dashed lines) at three locations and two time points.

Figure 12.
Idealized full aorta geometry and vessel wall material properties. **(a)**: coronal (left) and sagittal (right) views with lengths and diameters. **(b)**: close-up view of the arch and branches with lengths and diameters and the primary radius of curvature. **(c)**: close-up view of the arch showing the degree of curvature in the ascending arch (left) and transverse view of the arch (right), showing the degree of transverse curvature and the degree of angulation from the sagittal plane. **(d)**: the spatial distributions of wall thickness (*h*) and elastic modulus (*E*).

Figure 13.
Full aorta case. Flow rate (left) and pressure (right) with time at 8 outlets in the 3-D model (solid lines) and 1-D model (dashed lines) with relative error metrics (Section 2.6).
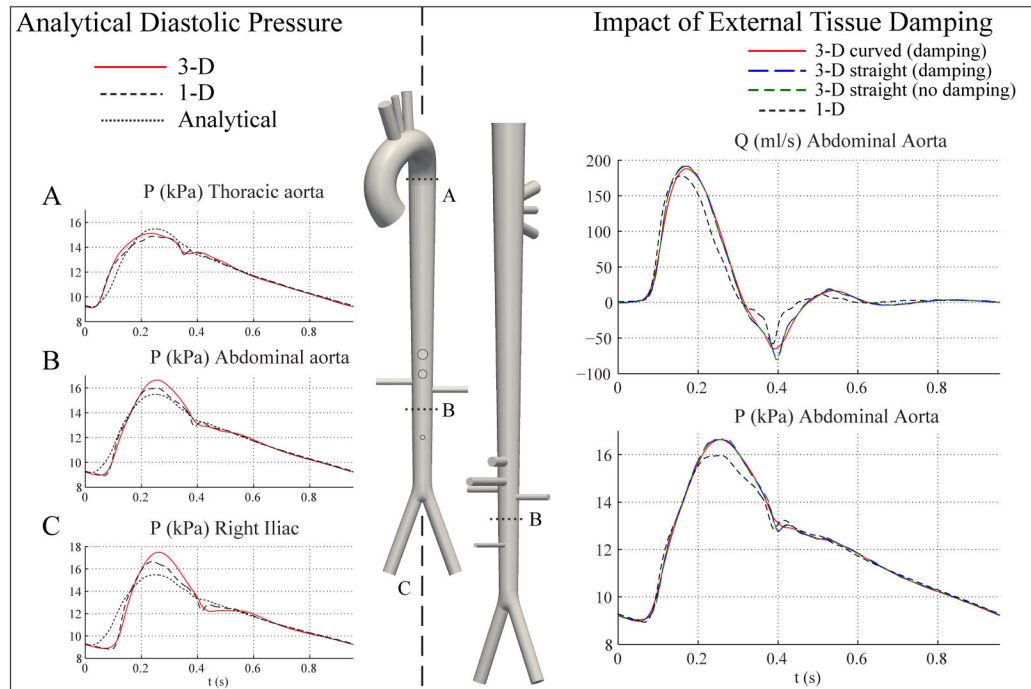
Figure 14.
Left: Analytical prediction of pressure (dotted lines) shows good agreement with 1-D and 3-D models during diastole. **Right**: Pressure and flow rate at the midpoint of the abdominal aorta for the curved 3-D aorta tree model with external damping (red), the straight 3-D aorta model with external damping (dashed blue), the straight 3-D aorta model without external damping (dashed green), and the 1-D model (dashed black). The level of external damping $c_s = 300$ Pa s m^{-1} and is identical for all the 3-D models.
The waveforms for the straight 3-D model with and without damping are essentially identical.

Table I

Normal hemodynamic properties of the human common carotid artery. The geometry, inflow rate and mechanical properties of the blood were taken from [17], the Young's modulus E from [65] and the pressures from [55, p. 343]. The parameters of the RCR windkessel model were calculated as described in the text. The resulting wave speed at mean pressure is $c_\mathrm{m} = 6.74$ m s^{-1}.

Property	Value
Length, L	126 mm
Radius at diastolic pressure, r_d	3 mm
Wall thickness, h	0.3 mm
Young's modulus, E	700.0 kPa
Mean flow rate, $\bar{Q_{in}}$	0.39 l min^{-1}
Systolic pressure, P_s	16.7 kPa
Diastolic pressure, P_d	10.9 kPa
Windkessel resistance, R_1	$2.4875 \cdot 10^8$ Pa s m^{-3}
Windkessel compliance, C	$1.7529 \cdot 10^{10}$ m^3 Pa^{-1}
Windkessel resistance, R_2	$1.8697 \cdot 10^9$ Pa s m^{-3}

Table II

Normal hemodynamic properties of the human aorta, from the ascending to the thoracic part. The inflow rate was taken from [50] and the pressures from [51]. The parameters of the RCR windkessel model were calculated as described in the text. The resulting wave speed at mean pressure is $c_m = 5.17$ m s^{-1}.

Property	Value
Length, L	24.137 cm
Radius at diastolic pressure, r_d	1.2 cm
Wall thickness, h	1.2 mm
Young's modulus, E	400.0 kPa
Mean flow rate, $\bar{Q}_{in}$	6.170 l min^{-1}
Systolic pressure, P_s	16.8 kPa
Diastolic pressure, P_d	9.5 kPa
Windkessel resistance, R_1	$1.1752 \cdot 10^7$ Pa s m^{-3}
Windkessel compliance, C	$1.0163 \cdot 10^8$ m^3 Pa^{-1}
Windkessel resistance, R_2	$1.1167 \cdot 10^8$ Pa s m^{-3}

Table III

Normal hemodynamic properties of the human aortic bifurcation. The dimensions are based on data given in [3]. The flow rate is taken from [66] and the pressures from [51]. The parameters of the two RCR models were calculated as described in the text. The resulting wave speed at mean pressure is $c_m = 6.26$ m s^{-1} in the abdominal aorta and $c_m = 7.4$ m s^{-1} in both iliac arteries.

Property	Aorta	Iliac
Length, L	8.6 cm	8.5 cm
Radius at diastolic pressure, r_d	0.86 cm	0.60 cm
Wall thickness, h	1.032 mm	0.72 mm
Young's modulus, E	500.0 kPa	700.0 kPa
Mean flow rate, $\bar{Q_{in}}$	0.4791 l min^{-1}	
Systolic pressure, P_s	16.8 kPa	
Diastolic pressure, P_d	9.5 kPa	
Windkessel resistance, R_1	–	$6.8123 \cdot 10^7$ Pa s m^{-3}
Windkessel compliance, C	–	$3.6664 \cdot 10^{10}$ m^3 Pa^{-1}
Windkessel resistance, R_2	–	$3.1013 \cdot 10^9$ Pa s m^{-3}

Table IV

Parameters of the full-aorta model. $r_{in} \rightarrow r_{out}$: diastolic cross-sectional radii at the inlet and outlet of the arterial segment. $c_{in} \rightarrow c_{out}$: wave speed at diastolic pressure at the inlet and outlet of the arterial segment.

Arterial segment	Length (cm)	$r_{in} \rightarrow r_{out}$ (mm)	$c_{in} \rightarrow c_{out}$ (m/s)	R_1 (10^7 Pa s m^{-3})	R_2 (10^8 Pa m^{-3})	C (10^{-10} m^3 Pa^{-1})
1. Ao I	7.0357	$15.2 \rightarrow 13.9$	$4.77 \rightarrow 4.91$	-	-	-
2. Ao II	0.8	$13.9 \rightarrow 13.7$	$4.91 \rightarrow 4.93$	-	-	-
3. Ao III	0.9	$13.7 \rightarrow 13.5$	$4.93 \rightarrow 4.94$	-	-	-
4. Ao IV	6.4737	$13.5 \rightarrow 12.3$	$4.94 \rightarrow 5.09$	-	-	-
5. Ao V	15.2	$12.3 \rightarrow 9.9$	$5.09 \rightarrow 5.43$	-	-	-
6. Ao VI	1.8	$9.9 \rightarrow 9.7$	$5.43 \rightarrow 5.46$	-	-	-
7. Ao VII	0.7	$9.7 \rightarrow 9.62$	$5.46 \rightarrow 5.48$	-	-	-
8. Ao VIII	0.7	$9.62 \rightarrow 9.55$	$5.48 \rightarrow 5.49$	-	-	-
9. Ao IX	4.3	$9.55 \rightarrow 9.07$	$5.49 \rightarrow 5.57$	-	-	-
10. Ao X	4.3	$9.07 \rightarrow 8.6$	$5.57 \rightarrow 5.66$	-	-	-
11. Brachiocephalic	3.4	$6.35 \rightarrow 6.35$	$6.20 \rightarrow 6.20$	5.1918	10.6080	8.6974
12. L com. carotid	3.4	$3.6 \rightarrow 3.6$	$7.36 \rightarrow 7.36$	19.1515	52.2129	1.7670
13. L subclavian	3.4	$4.8 \rightarrow 4.8$	$6.75 \rightarrow 6.75$	9.8820	13.0183	7.0871
14. Celiac	3.2	$4.45 \rightarrow 4.45$	$6.90 \rightarrow 6.90$	11.7617	7.5726	12.1836
15. Sup. mesenteric	6	$3.75 \rightarrow 3.75$	$7.27 \rightarrow 7.27$	17.4352	5.5097	16.7453
16. R renal	3.2	$2.8 \rightarrow 2.8$	$7.93 \rightarrow 7.93$	34.1378	5.3949	17.1017
17. L renal	3.2	$2.8 \rightarrow 2.8$	$7.93 \rightarrow 7.93$	34.1378	5.3949	17.1017
18. Inf. mesenteric	5	$2.0 \rightarrow 2.0$	$8.77 \rightarrow 8.77$	74.0167	46.2252	1.9959
19. R com. iliac	8.5	$6.0 \rightarrow 6.0$	$6.31 \rightarrow 6.31$	5.9149	10.1737	9.0686
20. L com. iliac	8.5	$6.0 \rightarrow 6.0$	$6.31 \rightarrow 6.31$	5.9149	10.1737	9.0686

Table V

Distribution of the cardiac output among each terminal vessel in the full aorta model.

Terminal vessel	% cardiac output
11. Brachiocephalic	10.41
12. L com. carotid	2.14
13. L subclavian	8.27
14. Celiac	13.24
15. Sup. mesenteric	15.97
16. R renal	13.15
17. L renal	13.15
18. Inf. mesenteric	2.16
19. R com. iliac	10.76
20. L com. iliac	10.76